

Assembly of functionally integrated human forebrain spheroids

Fikri Birey^{1*}, Jimena Andersen^{1*}, Christopher D. Makinson^{2*}, Saiful Islam³, Wu Wei^{3,4}, Nina Huber¹, H. Christina Fan⁵, Kimberly R. Cordes Metzler⁵, Georgia Panagiotakos⁶, Nicholas Thom¹, Nancy A. O'Rourke¹, Lars M. Steinmetz^{3,4,7}, Jonathan A. Bernstein⁸, Joachim Hallmayer¹, John R. Huguenard² & Sergiu P. Pasca¹

The development of the nervous system involves a coordinated succession of events including the migration of GABAergic (γ -aminobutyric-acid-releasing) neurons from ventral to dorsal forebrain and their integration into cortical circuits. However, these interregional interactions have not yet been modelled with human cells. Here we generate three-dimensional spheroids from human pluripotent stem cells that resemble either the dorsal or ventral forebrain and contain cortical glutamatergic or GABAergic neurons. These subdomain-specific forebrain spheroids can be assembled *in vitro* to recapitulate the saltatory migration of interneurons observed in the fetal forebrain. Using this system, we find that in Timothy syndrome—a neurodevelopmental disorder that is caused by mutations in the *Ca_v1.2* calcium channel—interneurons display abnormal migratory saltations. We also show that after migration, interneurons functionally integrate with glutamatergic neurons to form a microphysiological system. We anticipate that this approach will be useful for studying neural development and disease, and for deriving spheroids that resemble other brain regions to assemble circuits *in vitro*.

The formation of the human cerebral cortex involves the assembly of circuits composed of glutamatergic neurons, which are generated in the dorsal forebrain (pallium), and GABAergic interneurons, which are produced in the ventral forebrain (subpallium)^{1–3}. After specification, interneurons migrate long distances during human fetal development over several months and subsequently undergo activity-dependent maturation and integration into cortical circuits^{1,4}. Genetic or environmental perturbations of these processes can lead to an imbalance of cortical excitation and inhibition and this has been thought to contribute to neuropsychiatric disorders, including epilepsy and autism spectrum disorders (ASD)^{5,6}. These key developmental processes, which occur mostly in mid-to-late gestation, have been largely inaccessible for functional studies in humans^{7,8}. Moreover, the directed differentiation, and particularly the functional maturation, of cortical interneurons from human pluripotent stem (hPS) cells (induced pluripotent stem cells (hiPS cells) or embryonic stem cells (hES cells)), has been challenging^{9,10}. To date, no reliable, personalized models exist, to our knowledge, for the study of the migration of interneurons and their functional integration into human cortical ensembles.

Here, we leverage a three-dimensional differentiation approach using hPS cells to specify neural spheroids resembling the pallium (human cortical spheroids (hCS)) or the subpallium (human subpallium spheroids, (hSS)), and we subsequently assemble these spheroids *in vitro* to model for the first time the saltatory migration of human interneurons towards the cerebral cortex and their functional integration into microcircuits.

Generation of subdomain-specific forebrain spheroids

We have previously described the generation of floating, three-dimensional neural cultures from hPS cells resembling the pallium (hCS) that contain deep and superficial layer cortical glutamatergic

neurons, as well as astrocytes¹¹. To specify spheroids resembling the ventral forebrain or the subpallium (hSS), we exposed early spheroids, which were patterned by double SMAD inhibition, to small molecules that modulate the WNT and SHH pathways in the presence of the growth factors FGF2 and EGF (Fig. 1a and Supplementary Table 1). At day 25 of *in vitro* hSS differentiation, we observed a strong induction of the transcription factor *NKX2-1* in the hSS accompanied by high levels of *FOXG1* expression and downregulation of the pallial marker *EMX1*, suggestive of a subpallial fate (Fig. 1b and Supplementary Table 2). We next examined the hSS cytoarchitecture in cryosections and noticed that *NKX2-1* was expressed in ventricular zone-like structures at day 25 (Fig. 1c), but was distributed more broadly at later stages (Fig. 1d). At day 60, we observed strong expression of GABA and the GABA-synthesizing enzyme GAD67 in neurons (Fig. 1e, f). Of the known markers that identify GABAergic subtypes, somatostatin, calretinin and calbindin were the most strongly expressed; at later stages (after 200 days), and consistent with its expression later in development *in vivo*¹², parvalbumin was also present (Fig. 1g, h and Extended Data Fig. 1).

To comprehensively characterize the hSS and hCS, we performed single-cell transcriptional profiling at day 105 of differentiation using stochastic barcoding¹³ ($n = 11,838$ cells from hCS and hSS; BD Resolve system; Fig. 1i). Clustering of cells isolated from either the hCS or hSS using the t -distributed stochastic neighbour embedding (t SNE)¹⁴ approach revealed a separation of the two conditions. Neurons expressing *STMN2* were localized in the upper left of the t SNE space, whereas progenitors and mitotically active cells were distributed in the lower right (Extended Data Fig. 2a–c). Further examination identified several subdomains in the hCS (Fig. 1j and Extended Data Fig. 2d), including a group of glutamatergic neurons (*VGLUT1*⁺ (also known as *SLC17A7*)) expressing the cortical layer markers *TBR1*, *FEZF2* and *CTIP2* (also known as *BCL11B*); two groups of intermediate

¹Department of Psychiatry and Behavioral Sciences, Center for Sleep Sciences and Medicine, Stanford University School of Medicine, Stanford, California 94305, USA. ²Department of Neurology and Neurological Sciences, Stanford University School of Medicine, Stanford, California 94305, USA. ³Department of Genetics, Stanford University School of Medicine, Stanford, California 94305, USA. ⁴Stanford Genome Technology Center, Stanford University, Palo Alto, California 94304, USA. ⁵BD Genomics, Menlo Park, California 94025, USA. ⁶Department of Biochemistry and Biophysics, The Eli and Edythe Broad Center of Regeneration Medicine and Stem Cell Research, University of California, San Francisco, California 94143, USA. ⁷European Molecular Biology Laboratory (EMBL), Genome Biology Unit, 69117 Heidelberg, Germany. ⁸Department of Pediatrics, Stanford University School of Medicine, Stanford, California 94305, USA.

*These authors contributed equally to this work.

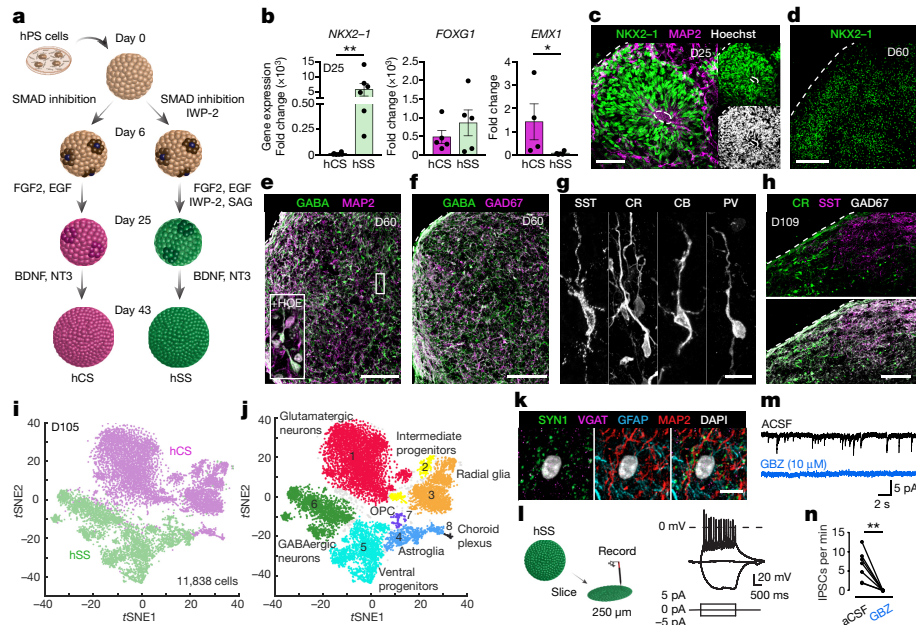


Figure 1 | Characterization of hSS derived from hPS cells. **a**, Generation of hCS and hSS. **b**, Fold changes (relative to gene expression in hPS cells; normalized to *GAPDH*) of *NKX2-1* ($n = 6$ hPS cell lines; Mann–Whitney U -test, $**P = 0.002$), *FOXG1* ($n = 5$ hPS cell lines; t -test, $P = 0.35$) and *EMX1* ($n = 4$ hPS cell lines; Mann–Whitney U -test, $*P = 0.02$) in hCS and hSS at day 25. **c–h**, Immunostaining of hSS for *NKX2-1* (**c**, **d**), GABA, GAD67 and MAP2 (**e**, **f**), and somatostatin (SST), calretinin (CR), calbindin (CB) and parvalbumin (PV) (**g**, **h**). **i**, **j**, Single-cell profiling of

hCS and hSS. **k**, Array tomography in hSS for MAP2, GFAP, SYN1 and VGAT. **l**, Patch clamping in a sliced hSS and a representative trace of a whole-cell current-clamp recording. **m**, **n**, Spontaneous IPSCs before (black) and during (blue) application of gabazine (GBZ) in an hSS slice (paired t -test, $**P = 0.004$). aCSF, artificial cerebrospinal fluid; HOE indicates Hoechst (inset in **e**). Data are mean \pm s.e.m. (**b**). Scale bars, 5 μ m (**k**), 20 μ m (**g**), 50 μ m (**c**), 100 μ m (**e**, **f**, **h**) and 200 μ m (**d**).

progenitors expressing *TBR2* (also known as *EOMES*), *INSM1* and *HES6*; and a group of dorsal progenitors expressing *LHX2*, *PAX6* and *GLAST1* (also known as *SLC1A3*) that also encompassed *HOPX*⁺ outer radial glia-like cells. By contrast, the hSS included a cluster of ventral neural progenitors, a group of GABAergic cells that expressed *DLX1*, *GAD1*, *VGAT* (also known as *SLC32A1*), *SCG2* and *SST*; and a small group of oligodendrocyte progenitors (*OLIG2* and *SOX10*) (Extended Data Fig. 2e–m and Supplementary Table 3). Astroglia from both the hCS and hSS clustered together and close to a small group of cells that resembled the choroid plexus (*TTR*⁺ and *SLC13A4*⁺). No cells with a mesodermal or endodermal identity were found.

We next explored the functional properties of the hSS. We found that seven days of exposure to the neurosteroid and GABA_A receptor agonist allopregnanolone combined with a three-day exposure to retinoic acid, significantly increased the frequency of spontaneous calcium spikes (Extended Data Fig. 3a–c). Notably, exposure to allopregnanolone with or without retinoic acid did not alter subpallial fate, neurotransmitter identity or the GABAergic subtypes in the hSS (Extended Data Fig. 3d–l). As a result, these two conditions were used for subsequent experiments. Considering the presence of spontaneous calcium activity and astrocytes (Fig. 1j), we investigated synaptogenesis in the hSS using array tomography. We found expression of the presynaptic protein synapsin-1 (SYN1) and the vesicular GABA transporter VGAT (Fig. 1k). We also used whole-cell patch clamping to record from neurons in sections of the hSS and found that approximately 75% of neurons generated action potentials in response to depolarization (Fig. 1l). At the same time, around 60% of neurons exhibit spontaneous inhibitory postsynaptic currents (IPSCs) that reverse in direction around the chloride reversal potential and are abolished by the GABA_A receptor antagonist gabazine (10 μ M) (Fig. 1m, n; in contrast to synaptic currents in the hCS, as shown in Extended Data Fig. 4).

Assembly of forebrain spheroids

To develop a model for the migration of interneurons into the cerebral cortex, we placed an hCS and hSS adjacent to each other inside a

conical tube (Fig. 2a). We used day 60 hCS that resembled the mid-gestation pallium¹¹, a developmental stage characterized by extensive migration of interneurons. After three days, the two spheroids fused (Fig. 2b). We used viral labelling of spheroids before assembly to monitor cell migration, and used a previously described DNA element near the *DLX1* and *DLX2* loci (*Dlx1/2b*) that labels medial ganglionic eminences and derivatives^{15,16}. Approximately 65% of *Dlx1/2b*::eGFP⁺ cells in the hSS expressed GAD67 and contained GABA and markers for GABAergic neuron subtypes (Extended Data Fig. 5a–d). We then used live cell imaging to monitor the position of *Dlx1/2b*::eGFP⁺ cells in fused hSS–hCS over multiple weeks. We observed a progressive movement of eGFP⁺ cells from the hSS into the hCS (Fig. 2c and Supplementary Video 1). This movement was specific to the fused hSS–hCS and unidirectional: we observed minimal movement either from the hCS into the hSS in a fused hSS–hCS or from the hSS into the hSS in a fused hSS–hSS (Fig. 2d and Extended Data Fig. 5e, f). The same pattern of migration could be observed for the hSS–hCS assembled at later stages (Extended Data Fig. 5g). When the hSS were plated on a coverslip, the migration was inefficient or absent (Extended Data Fig. 5h–j and Supplementary Video 2) similar to what has been reported in rodent cultures¹⁷. In the first 10 days after assembly, the vast majority of *Dlx1/2b*::eGFP⁺ cells that migrated away from the hSS had a leading process positioned towards the hCS at either a 45° or 90° angle relative to the interface (Extended Data Fig. 5k). At 30–50 days after assembly, 60% of the migrated cells were localized within the outer 100 μ m of the hCS (Extended Data Fig. 5l), and a large population of interneurons migrated into the hCS as shown by optical clearing (Fig. 2e). Notably, we also observed processes of *Dlx1/2b*::eGFP⁺ cells that briefly touched ventricular-zone-like regions, reminiscent of rodent ventricle-directed migration¹⁸ (Extended Data Fig. 5m–o and Supplementary Video 3). We next investigated the fate of *Dlx1/2b*::eGFP⁺ cells in the hSS after two weeks of migration from the hSS into hCS by isolating single cells and performing transcriptome analysis (Extended Data Fig. 6a). We found that the majority of migrated cells expressed subpallial markers (*DLX1*, *DLX2*, *DLX5* and

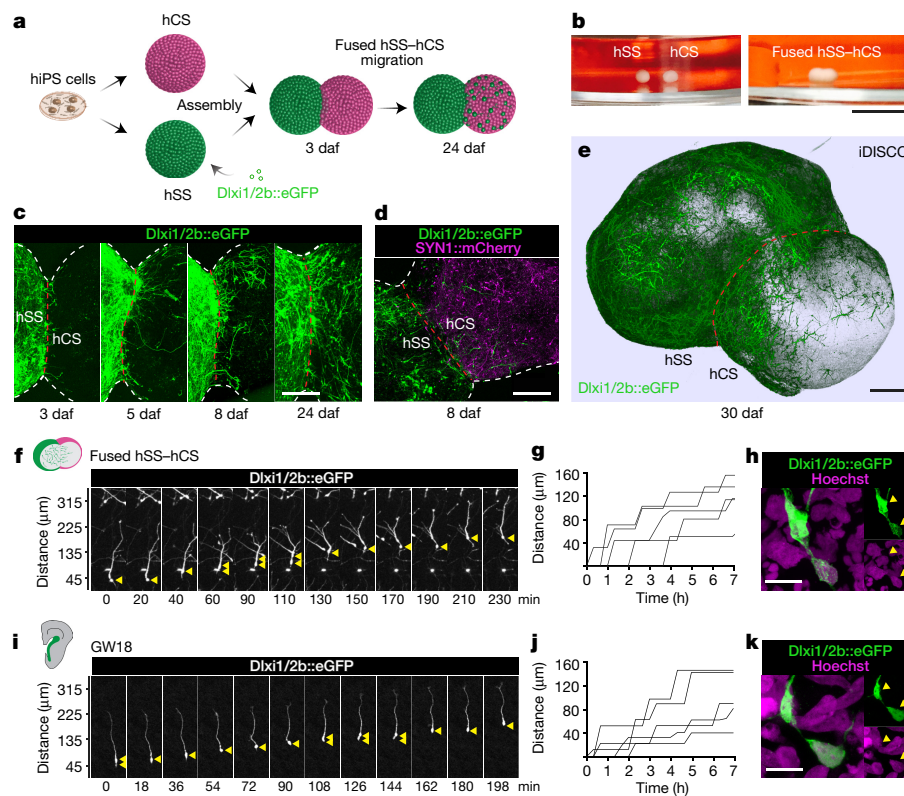


Figure 2 | Cell migration in fused hSS-hCS. **a**, Assembly of hCS and hSS. **daf**, days after fusion. **b**, Morphology before and after assembly. **c**, Time-lapse of migration from hSS into hCS. **d**, Assembly of hCS (AAV-hSYN1::mCherry) and hSS (lenti-Dlx1/2b::eGFP). **e**, Immunolabelling-enabled three-dimensional imaging of solvent-cleared organs (iDISCO)-

cleared hSS-hCS. Red dashed line indicates the border between hSS and hCS. **f-h**, Saltatory migration of Dlx1/2b::eGFP⁺ cells in fused hSS-hCS (**f, g**) and nucleokinesis (**h**). **i-k**, Saltatory migration of Dlx1/2b::eGFP⁺ cells in the human fetal forebrain (**i, j**) and nucleokinesis (**k**). Scale bars, 10 μ m (**h, k**), 50 μ m (**c**), 200 μ m (**d, e**) and 1 cm (**b**).

DLX6) and cortical interneuron markers (*GAD1*, *GAD2*, *VGAT* and *CELF4*) (Extended Data Figs 6b, 7a-d). We found few cells expressing *PAX6* or *TH*, which are indicative of olfactory interneurons; or *SP8*, *GSX2* or *CHAT*, which are indicative of striatal neurons, suggesting that the Dlx1/2b reporter is primarily labelling cortical interneurons (Extended Data Fig. 6b).

We next used confocal imaging to capture the movement of Dlx1/2b::eGFP⁺ cells in fused hSS-hCS. Interneurons moved in a saltatory pattern followed by extensive pauses (Fig. 2f). This characteristic, cyclical movement involved an extension of the leading process in one direction followed by a transient swelling of the soma and nuclear translocation (nucleokinesis; Fig. 2g, h). This pattern of migration is similar to that observed in rodents^{19,20}, although the ratio between the length of the leading process and the diameter of the soma in hSS-derived interneurons is almost double the ratio of mouse interneurons (Extended Data Fig. 8g-i). To validate the biological relevance of interneuron migration in hSS-hCS, we performed live cell imaging of cells labelled with the Dlx1/2b::eGFP reporter in human forebrain tissue (gestational weeks (GW)18 and GW20; Fig. 2i). Dlx1/2b::eGFP-labelled cells in fetal tissue co-expressed GABA and NKX2-1 (Extended Data Fig. 8a-f) and displayed a similar morphology and pattern of migration (Fig. 2j, k, Extended Data Fig. 8g-l and Supplementary Videos 4, 5).

We tested pharmacological manipulation of interneuron migration in fused hSS-hCS (Extended Data Fig. 7e). We imaged the movement of Dlx1/2b::eGFP⁺ cells before and after exposure to a CXCR4 receptor antagonist (AMD3100). This receptor is expressed in hSS (Extended Data Fig. 3l) and plays a key role in the migration of cortical interneurons²¹. AMD3100 treatment resulted in a significant reduction in saltation frequency, saltation length, speed when mobile (Extended Data Fig. 7f-h) and a change in path directness (Extended Data Fig. 7i, j and Supplementary Video 6).

Using assembled spheroids to model Timothy syndrome

We next investigated whether assembled hSS-hCS could be used to model migration defects. Previous work in rodents has indicated that L-type calcium channels (LTCCs) play a critical role in interneuron migration by regulating saltation frequency and migration termination¹⁷. LTCCs have been repeatedly associated with neuropsychiatric disorders^{22,23}, and gain-of-function mutations in the LTCC subunit-encoding *CACNA1C* gene lead to Timothy syndrome (TS)—a severe neurodevelopmental disease characterized by ASD and epilepsy^{24,25}. We generated hSS and hCS from hiPS cells from three patients with TS that carry the recurrent p.G406R substitution (Fig. 3a) and compared them to four control subjects (Extended Data Fig. 9a, b and Supplementary Table 1). We did not observe defects in the differentiation of TS hiPS cell lines into hSS (Extended Data Fig. 9c-g). Calcium imaging showed increased residual calcium following depolarization in hSS-derived TS neurons, as well as in hCS-derived TS neurons compared to control cells (Fig. 3b and Extended Data Fig. 9h, i), similar to what we have previously shown in TS hiPS cell-derived glutamatergic neurons²⁶. We investigated the migration of Dlx1/2b::eGFP⁺ cells in fused hSS-hCS (Fig. 3c, Extended Data Fig. 9j and Supplementary Video 7) and found an increase in saltation frequency in neurons from all three patients with TS (Fig. 3d and Extended Data Fig. 9k) consistent with the role of calcium in interneuron motility¹⁷. Notably, the saltation length and the speed when mobile were reduced in TS (Fig. 3e and Extended Data Fig. 9l, m) resulting in less efficient migration (Fig. 3f). Moreover, this effect was cell autonomous because migration of Dlx1/2b::eGFP⁺ cells from TS hSS into control hCS did not influence the phenotype (Fig. 3d, e and Extended Data Fig. 9k-m). To further validate these results, we electroporated cDNA encoding TS and wild-type Cav1.2 into slices of mouse embryonic day (E)14 ganglionic eminences and performed live cell imaging (Extended Data Fig. 9n, o). We observed a defect in mouse TS-Cav1.2 electroporated neurons

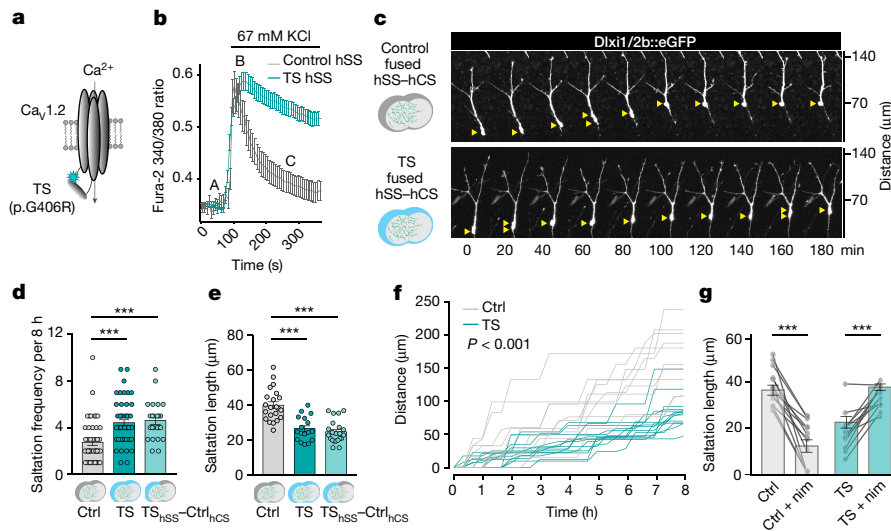


Figure 3 | Modelling of interneuron migration in fused hSS-hCS derived from patients with Timothy syndrome. **a**, TS mutation in $Ca_v1.2$. **b**, Calcium imaging in dissociated hSS (control (Ctrl), $n = 38$ cells from two subjects; TS, $n = 68$ cells from two subjects). **c**, Migration of $Dlx1/2b::eGFP^+$ cells in TS and control hSS-hCS. **d**, **e**, Number of saltations (control, $n = 48$ cells from three hiPS cell lines derived from three subjects; TS, $n = 51$ cells from three hiPS cell lines derived from three subjects; TS-control ($TS_{hSS}-Ctrl_{hCS}$) hybrid, $n = 24$ cells from five hiPS cell combinations from two TS and two control subjects), and saltation length (control, $n = 21$ cells from three hiPS cell lines derived from three subjects; TS, $n = 29$ cells from three hiPS cell lines derived from three subjects; TS-control ($TS_{hSS}-Ctrl_{hCS}$) hybrid, $n = 12$ cells from three

hiPS cell line combinations from two TS and three control subjects); one-way ANOVA with Dunnett's multiple comparison test ($***P < 0.001$). **f**, Migration of TS and control $Dlx1/2b::eGFP^+$ cells in fused hSS-hCS (two-way ANOVA, interaction $F_{24,408} = 17.71$, $P < 0.001$). **g**, Saltation length following exposure to nimodipine (nim) (paired t -test; control, $n = 13$ cells from three hiPS cell lines derived from three subjects, $***P < 0.001$; TS, $n = 12$ cells from two hiPS cell lines derived from two subjects, $***P < 0.001$). Data are mean \pm s.e.m., individual values are indicated by dots, which are paired when indicating before/after treatment. For details on the lines and number of cells used, see also Extended Data Fig. 9.

displaying more frequent but shorter saltations (Extended Data Fig. 9p, q). To determine whether the TS migratory phenotype was a result of LTCC activity and whether this could be reversed, we treated fused hSS-hCS with LTCC blockers (Fig. 3g and Extended Data Fig. 9r–u). We found that application of the LTCC blocker nimodipine significantly reduced saltation length and speed when mobile in control $Dlx1/2b::eGFP^+$ cells. However, the deficit in these parameters was rescued in TS $Dlx1/2b::eGFP^+$ cells following exposure to nimodipine. Moreover, roscovitine, a cyclin-dependent kinase inhibitor that increases voltage-dependent inactivation of $Ca_v1.2$ (refs 27, 28), also rescued saltation length in TS $Dlx1/2b::eGFP^+$ cells. These results indicate that the migration defect in interneurons carrying the TS gain-of-function mutation can be restored by reducing the activity of LTCCs.

Integration of interneurons in assembled spheroids

To investigate the hSS-derived neurons that migrated into hCS, we examined their single-cell transcriptome at four weeks after assembly (Fig. 4a). *t*SNE analysis indicated three clusters (Fig. 4b), whereby $Dlx1/2b::eGFP^+$ cells in the hSS were distributed primarily in cluster A, whereas $Dlx1/2b::eGFP^+$ cells that migrated into the hCS were primarily distributed in clusters B and C (Fig. 4c). Cells in all clusters expressed similar levels of *GAD1* and *CELFA*, but cluster B and C downregulated the subpallial marker *PBX3* (Extended Data Fig. 6c and Supplementary Table 4). Migrated cells displayed expression changes in genes that have previously been associated with interneuron migration, including *ERBB4*, *NNAT*, *MALAT1*, *SOX11* and *NXP1* (refs 29, 30) (Fig. 4d). These neurons also had higher levels of activity-dependent genes, including *FOS*, the AMPA-receptor trafficking regulator *GRIP2* (ref. 31) and *IGF1* (ref. 32), as well as the disease-related genes *RASD1* (ref. 33) and *TCF4* (ref. 34) (Fig. 4d and Extended Data Fig. 6c). We next examined dendrites of $Dlx1/2b::eGFP^+$ cells in hSS and in fused hSS-hCS. We found that hSS-derived cells that moved into hCS increased the complexity of their branching (Fig. 4e and Extended Data

Fig. 10a, b). We then measured their electrical properties in the hSS before and after assembly. We found that $Dlx1/2b::eGFP^+$ cells that had migrated into the hCS had double the maximum action potential generation rate as compared to $Dlx1/2b::eGFP^+$ cells in the unfused hSS or to non-migrated cells in the fused hSS-hCS (Fig. 4f and Extended Data Fig. 10c). We then assessed the integration of migrated neurons by using array tomography and observed the presence of gephyrin (GPHN), a postsynaptic protein localized to GABAergic synapses, in hCS that were fused to hSS but not in unfused hCS (Fig. 4g and Extended Data Fig. 10d). We constructed 'synptograms' consisting of a series of high-resolution sections through a single synapse, and found colocalization of eGFP from $Dlx1/2b$ -labelled cells with the presynaptic proteins SYN1 and VGAT and adjacent to the postsynaptic protein GPHN (Extended Data Fig. 10e). To investigate the presence of functional synapses in migrated $Dlx1/2b::eGFP^+$ neurons, we performed whole-cell voltage-clamp recordings in sliced hSS-hCS. We found that $Dlx1/2b::eGFP^+$ that migrated into the hCS display both excitatory and inhibitory postsynaptic currents (EPSCs (downward deflecting) and IPSCs (upward deflecting), respectively) (Fig. 4h). Moreover, after migration into the hCS, these cells primarily receive EPSCs rather than IPSCs and their synaptic input increases approximately threefold (Fig. 4i, Extended Data Fig. 10f and Supplementary Table 5). In parallel, glutamatergic neurons from hCS, which exhibit only EPSCs before assembly, also begin receiving IPSCs and show an overall increase in synaptic input following the migration of interneurons from the hSS (Fig. 4j and Extended Data Fig. 10g). To assess the functional integration of hCS and hSS neurons into neural networks, we applied electrical stimulation to the hCS side of the assembled hSS-hCS to trigger glutamate release from excitatory neurons in the vicinity of the stimulation electrode while simultaneously recording EPSCs and IPSCs in $Dlx1/2b::eGFP^+$ cells that migrated into the hCS (Extended Data Fig. 10h, i). We found that EPSCs were evoked immediately following electrical stimulation (>5 ms); this was followed by presumed multisynaptic IPSCs that were sensitive to

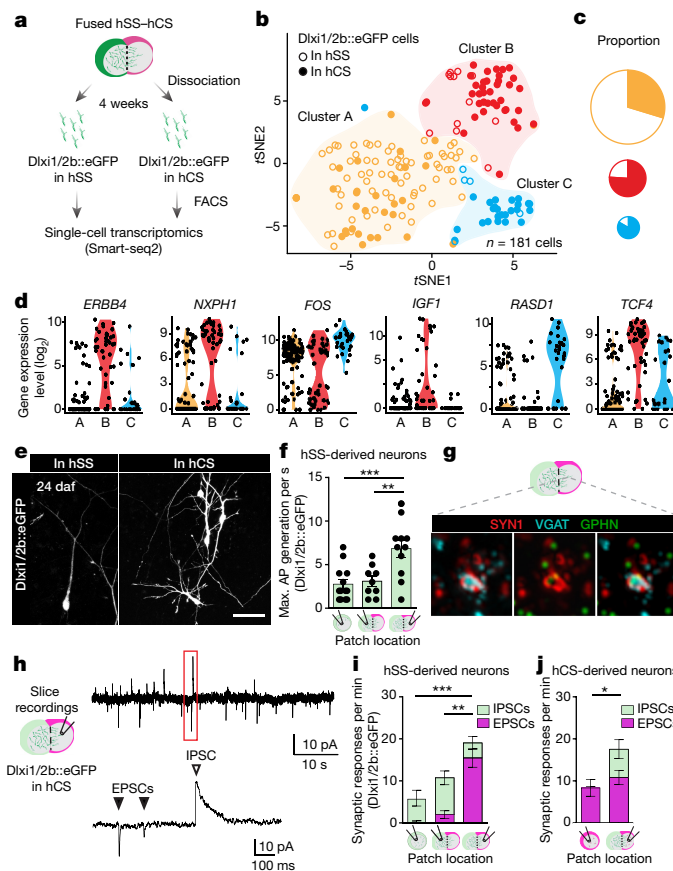


Figure 4 | Functional integration of interneurons in fused hSS-hCS. **a**, Isolation of Dlx1/2b::eGFP⁺ cells for transcriptomic analysis. **b**, tSNE visualization of single-cell gene expression at day 121 (four weeks after hSS-hCS assembly). **c**, Distribution across clusters (χ^2 test, $\chi^2 = 43.39$, $P < 0.0001$). **d**, Expression of *ERBB4*, *NXP1*, *FOS*, *IGF1*, *RASD1* and *TCF4*. **e**, Morphology of Dlx1/2b::eGFP⁺ cells before and after migration into hCS. **f**, Action potential generation in Dlx1/2b::eGFP⁺ cells (one-way ANOVA, $F_{2,30} = 1.25$; $P < 0.001$; Bonferroni post hoc test, $**P < 0.01$; $***P < 0.001$). **g**, A volume reconstruction ($4.0 \times 4.0 \times 2.1 \mu\text{m}$)

gabazine. Together, these data demonstrate that hSS integrate with hCS to assemble functional human microcircuits in three-dimensional cultures.

Discussion

We demonstrate the generation of a human three-dimensional microphysiological system that includes functionally integrated glutamatergic and GABAergic neurons. This platform has several advantages in comparison to previous adherent or three-dimensional methods^{9,10,16,35–38}. First, it involves the directed differentiation of subdomains of the forebrain that functionally interact in development. In contrast to whole-brain organoids and organoids resembling broader brain regions^{35,38}, this approach allows for modularity by combining separately patterned spheroids into multi-region neural three-dimensional cultures. Second, this system captures *in vitro* more elaborate developmental processes, including the saltatory migration of interneurons towards the cerebral cortex. Using live cell imaging of the human forebrain, we demonstrate that this migration is accurately recapitulated with our assembled three-dimensional platform. Third, by enabling their migration into an active neural network, interneurons integrate into a synaptically connected microphysiological system without the requirement of seeding onto rodent cortical cultures or brain slices. Assembling networks using this modular system may facilitate the study of excitation to inhibition interplay during cortical development.

We also demonstrate that forebrain subdomains derived from hiPS cells and fused *in vitro* can be used to identify the transcriptional

showing a GABAergic synapse (by array tomography) on the pallial side of a hSS-hCS stained for SYN1, GPHN and VGAT. **h**, EPSCs and IPSCs in Dlx1/2b::eGFP⁺ cells after migration. **i**, Synaptic responses in Dlx1/2b::eGFP⁺ cells (two-way ANOVA, interaction $F_{2,61} = 18.46$, $P < 0.0001$; Bonferroni post hoc test for EPSCs, $**P < 0.001$, $***P < 0.0001$). **j**, Synaptic responses in excitatory cells (two-way ANOVA, cortical neurons in hCS before and after assembly $F_{1,26} = 5.6$, $P < 0.05$; Bonferroni post hoc for IPSCs, $*P < 0.05$). Data are mean \pm s.e.m., individual values are indicated by dots. Scale bar, $50 \mu\text{m}$ (**e**).

changes associated with interneuron migration and to model disease processes that are otherwise inaccessible. We find that cortical interneurons derived from patients with TS display a cell-autonomous migration defect whereby they move more frequently but less efficiently. Moreover, the TS interneuron defect is rescued by pharmacologically manipulating LTCCs. This aberrant interneuron migration, taken together with our previous studies in cortical glutamatergic neurons^{26,39,40}, suggest the presence of abnormal cortical development and function in TS.

The *in vitro* specification of various subdomains of the developing human brain from hPS cells and their assembly into three-dimensional cultures open the opportunity for studying the interaction of specific neuronal cell types and for generating and probing neural circuits within personalized human microphysiological systems.

Online Content Methods, along with any additional Extended Data display items and Source Data, are available in the online version of the paper; references unique to these sections appear only in the online paper.

Received 8 December 2016; accepted 4 April 2017.

Published online 26 April 2017.

- Kepecs, A. & Fishell, G. Interneuron cell types are fit to function. *Nature* **505**, 318–326 (2014).
- Wonders, C. P. & Anderson, S. A. The origin and specification of cortical interneurons. *Nat. Rev. Neurosci.* **7**, 687–696 (2006).
- Silbereis, J. C., Pochareddy, S., Zhu, Y., Li, M. & Sestan, N. The cellular and molecular landscapes of the developing human central nervous system. *Neuron* **89**, 248–268 (2016).

4. Bartolini, G., Ciceri, G. & Marín, O. Integration of GABAergic interneurons into cortical cell assemblies: lessons from embryos and adults. *Neuron* **79**, 849–864 (2013).
5. Rubenstein, J. L. & Merzenich, M. M. Model of autism: increased ratio of excitation/inhibition in key neural systems. *Genes Brain Behav.* **2**, 255–267 (2003).
6. Marín, O. Interneuron dysfunction in psychiatric disorders. *Nat. Rev. Neurosci.* **13**, 107–120 (2012).
7. Tabar, V. & Studer, L. Pluripotent stem cells in regenerative medicine: challenges and recent progress. *Nat. Rev. Genet.* **15**, 82–92 (2014).
8. Paşca, S. P., Panagiotakos, G. & Dolmetsch, R. E. Generating human neurons *in vitro* and using them to understand neuropsychiatric disease. *Annu. Rev. Neurosci.* **37**, 479–501 (2014).
9. Maroof, A. M. *et al.* Directed differentiation and functional maturation of cortical interneurons from human embryonic stem cells. *Cell Stem Cell* **12**, 559–572 (2013).
10. Nicholas, C. R. *et al.* Functional maturation of hPSC-derived forebrain interneurons requires an extended timeline and mimics human neural development. *Cell Stem Cell* **12**, 573–586 (2013).
11. Paşca, A. M. *et al.* Functional cortical neurons and astrocytes from human pluripotent stem cells in 3D culture. *Nat. Methods* **12**, 671–678 (2015).
12. Uylings, H. B. M., Delalle, I., Petanjek, Z. & Koenderink, M. J. T. Structural and immunocytochemical differentiation of neurons in prenatal and postnatal human prefrontal cortex. *Neuroembryology* **1**, 176–186 (2002).
13. Fan, H. C., Fu, G. K. & Fodor, S. P. Expression profiling. Combinatorial labeling of single cells for gene expression cytometry. *Science* **347**, 1258367 (2015).
14. van der Maaten, L. & Hinton, G. Visualizing data using t-SNE. *J. Mach. Learn. Res.* **9**, 2579–2605 (2008).
15. Potter, G. B. *et al.* Generation of Cre-transgenic mice using *Dlx1/Dlx2* enhancers and their characterization in GABAergic interneurons. *Mol. Cell. Neurosci.* **40**, 167–186 (2009).
16. Sun, Y. *et al.* A deleterious $Na_v1.1$ mutation selectively impairs telencephalic inhibitory neurons derived from Dravet syndrome patients. *eLife* **5**, e13073 (2016).
17. Bortone, D. & Polleux, F. KCC2 expression promotes the termination of cortical interneuron migration in a voltage-sensitive calcium-dependent manner. *Neuron* **62**, 53–71 (2009).
18. Nadarajah, B., Alifragis, P., Wong, R. O. & Parnavelas, J. G. Ventricle-directed migration in the developing cerebral cortex. *Nat. Neurosci.* **5**, 218–224 (2002).
19. Anderson, S. A., Marín, O., Horn, C., Jennings, K. & Rubenstein, J. L. Distinct cortical migrations from the medial and lateral ganglionic eminences. *Development* **128**, 353–363 (2001).
20. Bellion, A., Baudoin, J. P., Alvarez, C., Bornens, M. & Métin, C. Nucleokinesis in tangentially migrating neurons comprises two alternating phases: forward migration of the Golgi/centrosome associated with centrosome splitting and myosin contraction at the rear. *J. Neurosci.* **25**, 5691–5699 (2005).
21. Stumm, R. K. *et al.* CXCR4 regulates interneuron migration in the developing neocortex. *J. Neurosci.* **23**, 5123–5130 (2003).
22. Cross-Disorder Group of the Psychiatric Genomics Consortium. Identification of risk loci with shared effects on five major psychiatric disorders: a genome-wide analysis. *Lancet* **381**, 1371–1379 (2013).
23. Schizophrenia Working Group of the Psychiatric Genomics Consortium. Biological insights from 108 schizophrenia-associated genetic loci. *Nature* **511**, 421–427 (2014).
24. Splawski, I. *et al.* $Ca_v1.2$ calcium channel dysfunction causes a multisystem disorder including arrhythmia and autism. *Cell* **119**, 19–31 (2004).
25. Splawski, I. *et al.* Severe arrhythmia disorder caused by cardiac L-type calcium channel mutations. *Proc. Natl Acad. Sci. USA* **102**, 8089–8096 (2005).
26. Paşca, S. P. *et al.* Using iPSC-derived neurons to uncover cellular phenotypes associated with Timothy syndrome. *Nat. Med.* **17**, 1657–1662 (2011).
27. Yarotsky, V. *et al.* Roscovitine binds to novel L-channel ($Ca_v1.2$) sites that separately affect activation and inactivation. *J. Biol. Chem.* **285**, 43–53 (2010).
28. Yarotsky, V. & Elmslie, K. S. Roscovitine, a cyclin-dependent kinase inhibitor, affects several gating mechanisms to inhibit cardiac L-type ($Ca_v1.2$) calcium channels. *Br. J. Pharmacol.* **152**, 386–395 (2007).
29. Zechel, S., Zajac, P., Lönnerberg, P., Ibáñez, C. F. & Linnarsson, S. Topographical transcriptome mapping of the mouse medial ganglionic eminence by spatially resolved RNA-seq. *Genome Biol.* **15**, 486 (2014).
30. Batista-Brito, R., Machold, R., Klein, C. & Fishell, G. Gene expression in cortical interneuron precursors is prescient of their mature function. *Cereb. Cortex* **18**, 2306–2317 (2008).
31. Mao, L., Takamiya, K., Thomas, G., Lin, D. T. & Huganir, R. L. GRIP1 and 2 regulate activity-dependent AMPA receptor recycling via exocyst complex interactions. *Proc. Natl Acad. Sci. USA* **107**, 19038–19043 (2010).
32. Mardinly, A. R. *et al.* Sensory experience regulates cortical inhibition by inducing IGF1 in VIP neurons. *Nature* **531**, 371–375 (2016).
33. Lacaria, M., Gu, W. & Lupski, J. R. Circadian abnormalities in mouse models of Smith–Magenis syndrome: evidence for involvement of *RAI1*. *Am. J. Med. Genet. A* **161**, 1561–1568 (2013).
34. Blake, D. J. *et al.* *TCF4*, schizophrenia, and Pitt–Hopkins syndrome. *Schizophr. Bull.* **36**, 443–447 (2010).
35. Lancaster, M. A. *et al.* Cerebral organoids model human brain development and microcephaly. *Nature* **501**, 373–379 (2013).
36. Mariani, J. *et al.* Modeling human cortical development *in vitro* using induced pluripotent stem cells. *Proc. Natl Acad. Sci. USA* **109**, 12770–12775 (2012).
37. Kadoshima, T. *et al.* Self-organization of axial polarity, inside-out layer pattern, and species-specific progenitor dynamics in human ES cell-derived neocortex. *Proc. Natl Acad. Sci. USA* **110**, 20284–20289 (2013).
38. Qian, X. *et al.* Brain-region-specific organoids using mini-bioreactors for modeling ZIKV exposure. *Cell* **165**, 1238–1254 (2016).
39. Krey, J. F. *et al.* Timothy syndrome is associated with activity-dependent dendritic retraction in rodent and human neurons. *Nat. Neurosci.* **16**, 201–209 (2013).
40. Tian, Y. *et al.* Alteration in basal and depolarization induced transcriptional network in iPSC derived neurons from Timothy syndrome. *Genome Med.* **6**, 75 (2014).

Supplementary Information is available in the online version of the paper.

Acknowledgements We thank J. Y. Park, K. Sabatini, T. Khan, S. Yoon, H. Gai and L. Elahi at Stanford University, R.E. Dolmetsch at Novartis Institutes for Biomedical Research, and N. Bansal and J. Fan at BD Genomics for advice and support. This work was supported by grants from NIH/National Institute of Mental Health (NIMH) grants R01MH100900 and R01MH100900-02S1, NIMH BRAINS Award R01MH107800, the California Institute of Regenerative Medicine (CIRM), the MQ Fellow Award, the Donald E. and Delia B. Baxter Foundation Faculty Award, the Kwan Research Fund and Stanford Start-up Funds (to S.P.P.), Child Research Health Institute Postdoctoral Fellowship (CHR) (to F.B., N.H.), Walter V. and Idun Berry Postdoctoral Fellowship (to J.A.) and the Stanford Medicine Dean’s Fellowship (to F.B., J.A., N.H.), the American Epilepsy Society and Wishes for Elliott Foundation Fellowship (to C.D.M.), NIH 5P01HG00020526 (to L.M.S.), the UCSF Program for Breakthrough Biomedical Research and Sandler Foundation (to G.P.).

Author Contributions F.B. and J.A. developed the differentiation platform and assays. C.D.M. and J.R.H. designed, conducted and analysed the electrophysiological experiments. F.B., J.A., N.H. and N.T. contributed to neural differentiation, live cell imaging experiments and analysis. F.B. and J.A. were able to replicate the differentiation and spheroid assembly independently. S.I., W.W., H.C.F., K.R.C.M. and L.M.S. contributed to the single-cell experiments. N.A.O. performed the array tomography. J.A.B. and J.H. recruited and characterized the subjects. G.P., J.A. and F.B. performed or analysed the electroporation experiments. F.B., J.A. and S.P.P. conceived the project, designed experiments and wrote the paper with input from all authors. S.P.P. supervised all aspects of the work.

Author Information Reprints and permissions information is available at www.nature.com/reprints. The authors declare competing financial interests: details are available in the online version of the paper. Readers are welcome to comment on the online version of the paper. Publisher’s note: Springer Nature remains neutral with regard to jurisdictional claims in published maps and institutional affiliations. Correspondence and requests for materials should be addressed to S.P.P. (spasca@stanford.edu).

Reviewer Information *Nature* thanks G. Fishell, A. Goffinet and B. Treutlein for their contribution to the peer review of this work.

METHODS

Culture of hPS cells. The hPS cell lines used in this study were validated using standardized methods as previously described^{26,41}. Cultures were tested for and maintained mycoplasma free. A total of six control hiPS cell lines derived from fibroblasts collected from five subjects (two males and three females), plus the human embryonic stem cell line H9, and seven hiPS cell lines derived from fibroblasts collected from three subjects with TS (one female and two males) carrying the p.G406R mutation were used for experiments (Supplementary Table 1; subjects 7643 and 9862 are from refs 26, 41). The TS point mutation in exon 8a of *CACNA1C* was verified by PCR as previously described⁴¹. The hiPS cell line H20961 was derived by the Gilad laboratory⁴². Approval for this study was obtained from the Stanford IRB panel and informed consent was obtained from all subjects.

Generation from hPS cells of hCS and hSS. hPS cells (hiPS or hES cells) were cultured on inactivated mouse embryonic fibroblast feeders (EmbryoMax PMEF; Millipore) in hPS cell medium containing DMEM/F12 (1:1, Life Technologies, 11330), knockout serum (20%, Life Technologies, 10828), non-essential amino acids (1 mM, Life Technologies, 11140), GlutaMax (1:200, Life Technologies, 35050), β -mercaptoethanol (0.1 mM, Sigma-Aldrich, M3148), penicillin and streptomycin (1:100, Life Technologies, 15070), and supplemented with FGF2 (10 ng ml^{-1} diluted in 0.1% BSA; R&D Systems).

The generation of hCS from hPS cells was performed as previously described¹¹. To initiate the generation of hCS or hSS, intact hiPS cell colonies were lifted from the plates using dispase (0.35 mg ml^{-1}) and transferred into ultralow-attachment plastic dishes (Corning) in hPS cell medium supplemented with the two SMAD inhibitors dorsomorphin ($5\text{ }\mu\text{M}$, Sigma-Aldrich) and SB-431542 ($10\text{ }\mu\text{M}$, Tocris), and the ROCK inhibitor Y-27632 ($10\text{ }\mu\text{M}$, EMD Chemicals). For the first five days, the hPS cell medium was changed every day and supplemented with dorsomorphin and SB-431542. On the sixth day in suspension, neural spheroids were transferred to neural medium containing neurobasal-A (Life Technologies, 10888), B-27 supplement without vitamin A (Life Technologies, 12587), GlutaMax (1:100, Life Technologies), penicillin and streptomycin (1:100, Life Technologies) and supplemented with the growth factors EGF (20 ng ml^{-1} ; R&D Systems) and FGF2 (20 ng ml^{-1} ; R&D Systems) until day 24. For the generation of hSS, the medium was supplemented with additional small molecules during the first 23 days in culture; a schematic showing the recipes is presented in Extended Data Fig. 3a. For the hSS-IS condition the following reagents were added in addition to those described above: the Wnt pathway inhibitor IWP-2 (inhibitor of WNT production-2, $5\text{ }\mu\text{M}$, Selleckchem) from day 4 until day 24, and the SHH pathway agonist SAG (smoothed agonist, 100 nM , Selleckchem) from day 12 to day 24. The hSS-ISA condition also included IWP-2 and SAG with the addition of allopregnanolone (100 nM , Cayman Chemicals) from day 15 to day 24, and the hSS-ISRA condition also included IWP-2 and SAG, and additionally, allopregnanolone (100 nM) from day 15–24, and a brief exposure (day 12–15) to retinoic acid (100 nM , Sigma-Aldrich). From day 25 to 42, the neural medium for both the hCS and hSS conditions, was supplemented with the growth factors BDNF (20 ng ml^{-1} , Peprotech) and NT3 (20 ng ml^{-1} , Peprotech) with medium changes every other day. From day 43 onwards, hCS and hSS were maintained in unsupplemented neural medium with medium changes every four to six days. A step-by-step protocol describing subdomain-specific forebrain spheroids generation and assembly can be found at Protocol Exchange⁴³.

Viral labelling and assembly of neural spheroids. The viral infection of the three-dimensional neural spheroids was performed as previously described^{11,44}. In brief, hCS or hSS were transferred to a 1.5-ml microcentrifuge Eppendorf tube containing $300\text{ }\mu\text{l}$ neural medium with virus and incubated overnight. The next day, neural spheroids were transferred into fresh neural medium in ultralow attachment plates. Lentivirus (lenti-Dlx1/2b::eGFP; construct reported and applied in refs 15, 16 and received from J. L. Rubenstein) was generated by transfecting HEK293T cells with Lipofectamine 2000 (Thermo Fisher Scientific) and concentrating the supernatant with the Lenti-X concentrator (Clontech) 72 h later. Adenovirus (AAV-DJ1-hSYN1::mCherry) was generated in the Stanford Gene Vector and Virus Core at Stanford University School of Medicine.

To assemble the forebrain spheroids, hCS and hSS (around 60 to 90 days of *in vitro* differentiation), which were virally labelled 8–10 days before, were transferred to a 1.5-ml microcentrifuge Eppendorf tube for three days and placed in an incubator. During this time, more than 95% of the hCS and hSS fused. These hSS–hCS cultures were carefully transferred into 24-well ultralow-attachment plates (Corning) using a cut P1000 pipette tip and medium changes were performed very gently every two to three days.

Cryopreservation. hCS were fixed in 4% paraformaldehyde (PFA) and 8% sucrose for 30 min to 2 h. They were then washed in PBS, transferred to 15% sucrose solution overnight at $4\text{ }^{\circ}\text{C}$ and then to 30% sucrose for 48–72 h. Subsequently, they were transferred into embedding medium (Tissue-Tek OCT Compound 4583, Sakura Finetek), snap-frozen on dry ice and stored at $-80\text{ }^{\circ}\text{C}$. For

immunohistochemistry, 10- to 20- μm -thick sections were cut using a cryostat (Leica). Human brain tissue was fixed in 4% PFA for 48 h, washed in PBS and transferred to 30% sucrose for one week. Sections were then embedded in OCT and 30% sucrose (1:1) and sectioned into 30- μm sections using a Leica cryostat.

Immunohistochemistry. Cryosections were washed with PBS to remove excess OCT and blocked in 10% normal goat serum (NGS), 0.3% Triton X-100 diluted in PBS for 1 h at room temperature. The sections were then incubated overnight at $4\text{ }^{\circ}\text{C}$ with primary antibodies diluted in PBS containing 10% NGS and 0.3% Triton X-100. PBS was used to wash off the primary antibodies and the cryosections were incubated with secondary antibodies in PBS with 10% NGS and 0.3% Triton X-100 for 1 h. The following primary antibodies were used for immunohistochemistry: anti-NKX2-1 (rabbit, 1:200, Santa Cruz, sc-13040), anti-MAP2 (guinea pig, 1:1,000, Synaptic Systems, 188004), anti-GABA (rabbit, 1:1,000, Sigma-Aldrich, A2052), anti-GAD67 (mouse, 1:1,000, Millipore, MAB5406), anti-somatostatin (rat, 1:200, Millipore, MAB354), anti-calretinin (rabbit, 1:1,000, Swant, CR7697), anti-calbindin (rabbit, 1:1,000, Swant, CB38), anti-parvalbumin (rabbit, 1:6,000, Swant, PV27), anti-parvalbumin (mouse 1:1,000, Millipore, MAB1572), anti-GFP (chicken, 1:1,500, GeneTex, GTX13970), anti-DCX (guinea pig, 1:1,000, Millipore, AB2253); anti-TBR1 (rabbit, 1:200, Abcam, AB31940), anti-GFAP (rabbit, 1:1,000, DAKO, Z0334), anti-CTIP2 (rat, 1:300, Abcam, AB18465), anti-OCT4 (rabbit, 1:200, Cell Signaling Technology), anti-SSEA4 (mouse, 1:200, Cell Signaling Technology). Alexa Fluor dyes (Life Technologies) were used at 1:1,000 dilution for amplification of the signal. Nuclei were visualized with Hoechst33258 (Life Technologies). Cryosections were mounted for microscopy on glass slides using Aquamount (Thermo Scientific) and imaged on a Zeiss M1 Axioscope or Leica TCS SP8 confocal microscope. Images were processed in ImageJ (Fiji).

Dissociation of hCS and hSS. For the enzymatic dissociation of hCS and hSS for culture in monolayer and immunocytochemistry, spheroids were incubated with Accutase (Innovative Cell Technologies) for 25 min at $37\text{ }^{\circ}\text{C}$, washed with neural medium and gently triturated using a P200 pipette. Cells were plated on glass coverslips (15 mm, Warner Instruments) coated with poly-L-ornithine and laminin (Sigma-Aldrich) at a density of around 1 spheroid per two coverslips in neural medium supplemented with BDNF and NT3.

To dissociate hCS and hSS for single-cell profiling, we adapted a previously published protocol used for primary human fetal brain tissue⁴⁵. In brief, up to six spheroids were chopped using a #10 blade and then incubated in papain enzyme solution (27.3 U ml^{-1} , Worthington), EBSS ($1\times$, Sigma-Aldrich), 0.46% sucrose (Sigma-Aldrich), 26 mM NaHCO_3 (Sigma-Aldrich), 0.5 mM EDTA (Sigma-Aldrich) at $37\text{ }^{\circ}\text{C}$ for 70 min in an incubator ($5\text{ }\text{CO}_2$). The digested spheroids were then washed and carefully triturated in a trypsin inhibitor solution containing EBSS, 0.46% sucrose (Sigma-Aldrich), 26 mM NaHCO_3 (Sigma-Aldrich), $15\text{--}30\text{ mg trypsin inhibitor}$ (Sigma-Aldrich). After centrifugation, the pellet was resuspended in 0.2% BSA diluted in PBS and supplemented with Y-27632 ($10\text{ }\mu\text{M}$, EMD Chemicals) and the cells were used for fluorescence-activated cell sorting (FACS).

Mouse slice cultures. Organotypic cultures of mouse coronal forebrain slices were prepared following published methods⁴⁶ with some modifications. Whole brains from E14–E18 mouse embryos were embedded in 4% low-melting point agarose and slices were cut at $250\text{--}300\text{ }\mu\text{m}$ using a Leica VT1200 vibrotome in complete HBSS (100 ml of $10\times$ HBSS without Ca or Mg, 2.5 ml of 1 M HEPES buffer at pH 7.4, 30 ml of 1 M D-glucose, 10 ml of 100 mM CaCl_2 , 10 ml of 100 mM MgSO_4 and 4 ml of 1 M NaHCO_3). Slices with visible forebrain structures were placed in membrane inserts (diameter, 13 mm; pore size, $8\text{ }\mu\text{m}$; Costar) coated with poly-L-ornithine and laminin (Sigma-Aldrich) overnight. They were cultured in a Basal Medium Eagle (39 ml, Life Technologies, 21010046) supplemented with 12.9 ml of complete HBSS, 1.35 ml of 1 M D-glucose, $250\text{ }\mu\text{l}$ of 200 mM GlutaMax (Life Technologies) and 5% heat-inactivated horse serum (Life Technologies, 26050070). Slices were imaged using a Leica SP8 confocal microscope. Approval for mouse experiments was obtained from the Stanford University's Administrative Panel on Laboratory Animal Care (APLAC).

Electroporation of mouse slices. Coronal slices of mouse embryonic forebrain at E14 were prepared as described above. Sections were transferred into tissue-culture dishes containing complete HBSS for approximately 1 h, after which CAG-Cav1.2 (wild-type- or TS-CACNA1C) plasmids were focally co-injected with CAG::GFP at a ratio of 1:0.5 directly into the ganglionic eminence through a glass micropipette. Cav1.2-overexpression constructs were generated by insertion of PCR-amplified wild-type- and TS-Cav1.2 coding sequences from dihydropyridine-insensitive Cav1.2 constructs³⁹ into pCAGIG (gift from C. Cepko through Addgene, plasmid 11159)⁴⁷. Slices were then electroporated using two horizontally oriented platinum electrodes powered by a BTX Square Pulse Electroporator and placed onto cell-culture membrane inserts for subsequent live cell imaging 48 h later as described below.

Human tissue. Human tissue was obtained under a protocol approved by the Research Compliance Office at Stanford University. The tissue was processed

using an adapted protocol⁴⁸. In brief, GW18 or GW20 frontal brain tissue was embedded in 4% low-melting point agarose in bubbled artificial cerebrospinal fluid (aCSF: 125 mM NaCl, 2.5 mM KCl, 1 mM MgCl₂, 2 mM CaCl₂, 1.25 mM NaH₂PO₄, 25 mM NaHCO₃, 25 mM D-(+)-glucose) and either sectioned using a Leica VT1200 Vibratome at 300–500 μm in ice-cold, bubbled aCSF, or cut using the sharp end of a 22-gauge needle to obtain 1–2-mm thick sections. The sections were then placed in tissue-culture plates containing culture medium (66% BME, 25% Hanks, 5% FBS, 1% N-2, 1% penicillin, streptomycin and glutamine; all from Invitrogen) and 0.66% D-(+)-glucose (Sigma-Aldrich) and incubated (37 °C, 5% CO₂) with the Dlx1/2b::eGFP lentivirus for 30 min to 1 h. Sections were then transferred to cell-culture membrane inserts (diameter, 13 mm; pore size, 8 μm; Costar) and incubated in culture medium at 37 °C, 8% O₂, 5% CO₂ for up to eight days. Half media changes were performed every other day. After around 5 days in culture, Dlx1/2b::eGFP⁺ cells could be detected and were subsequently imaged as described below.

Live cell imaging and analysis of Dlx1/2b::eGFP⁺ cell migration. The migration of Dlx1/2b::eGFP⁺ cells was imaged for 8–12 h under environmentally controlled conditions (37 °C, 5% CO₂) in intact, fused hSS–hCS using a confocal microscope with a motorized stage (Leica SP8). Fused hSS–hCS were transferred to a well of a 96-well plate (glass-bottom plates, Corning) in 200 μl of neural medium. Spheroids were incubated in an environmentally controlled chamber for 30–60 min before imaging. During a given recording session, up to eight fused hSS–hCS were imaged at a depth of 50–150 μm and at a rate of 15–20 min per frame. For pharmacological manipulation, cells were imaged for 12 h to record a baseline. Then, the medium was carefully removed and new medium with small molecules (AMD3100 at 100 nM; nimodipine at 5 μM; or roscovitine at 15 μM) was gently added to the well. The field of view was readjusted to capture the previous region of interest and cells in fused hSS–hCS were imaged for an additional 12 h.

For imaging of Dlx1/2b::eGFP⁺ cells, E17–E18 slices were placed on inserts and infected with Dlx1/2b::eGFP lentivirus after 24 h. The slices were imaged two days later using a Leica SP8 confocal microscope (see above).

For measuring the branch to soma length ratio of human cells on mouse slices, hSSs infected with Dlx1/2b::eGFP lentivirus were dissociated and placed on top of E13–E14 mouse slices, which were placed on cell-culture inserts 8–24 h before. The hSS-derived Dlx1/2b::eGFP⁺ cells were imaged with the Leica SP8 confocal microscope system at least 48 h later.

The migration of mouse Dlx1/2b::eGFP⁺ cells or Ca_v1.2-electroporated cells and the migration of human fetal Dlx1/2b::eGFP-infected cells were both imaged with the same settings described for intact, fused hSS–hCS. Slices were kept on the cell culture inserts during imaging.

For quantification of migration of Dlx1/2b::eGFP⁺ cells after plating on coverslips, intact hSS were plated on glass coverslips (15 mm, Warner Instruments) coated with poly-L-ornithine and laminin (Sigma-Aldrich). Cells were imaged 7–10 days after using a confocal microscope (Leica SP8) as described above.

ImageJ and the Chemotaxis & Migration Tool (Ibidi) were used for the post-acquisition analysis of cell mobility. The StackReg plugin in ImageJ was used to correct for minor drifts during imaging. To estimate the length of individual saltations, Dlx1/2b::eGFP cells displaying a swelling of the soma were identified, and distance (in μm) to the new position of the soma following nucleokinesis was recorded manually. The time necessary for this movement was used to calculate the speed when mobile. To estimate the directness of the movement, the *x* and *y* coordinates of each cell per frame and time were extracted with the manual tracking plugin (ImageJ) and the Chemotaxis & Migration Tool (Ibidi) was used to calculate the accumulated (*A*) and Euclidian (*E*) distances travelled per cell over time. Path directness was calculated as the *E/A* ratio. Videos were processed using ImageJ and Final Cut Pro X.

Fura-2 calcium imaging of hSS or hCS cultures. Dissociated hSS (day 62) or hCS (day 123) derived from control and TS lines were cultured for 4–5 days on glass coverslips (15 mm, Warner Instruments) coated with poly-L-ornithine and laminin (Sigma-Aldrich). The cultures were incubated with 1 μM Fura-2 acetoxymethyl ester (Fura-2 AM, Invitrogen) for 25 min at 37 °C in neural medium, washed for 5 min and placed in a perfusion chamber on the stage of an inverted fluorescence microscope (TE2000U, Nikon). Cells were then stimulated with high-KCl Tyrode's solution (67 mM KCl, 67 mM NaCl, 2 mM CaCl₂, 1 mM MgCl₂, 30 mM glucose and 25 mM HEPES, pH 7.4). Imaging was performed at room temperature (25 °C) on an epifluorescence microscope equipped with an excitation filter wheel and an automated stage. Openlab software (PerkinElmer) was used to collect and quantify time-lapse excitation ratio images. Fluorescence images were analysed using the IGOR Pro software (WaveMetrics). Residual calcium following high-KCl depolarization was calculated by dividing the plateau calcium level by the peak calcium elevation ((*C* – *A*) / (*B* – *A*), Fig. 3b).

Fluo-4 calcium imaging in intact hSS. Intact hSS at day 43–52 were incubated with 10 μM Fluo-4 acetoxymethyl ester (Fluo-4 AM, Invitrogen) for 30 min in

neural medium followed by a 15 min wash with neural medium. A Leica SP8 confocal microscope with a resonant scanner was used for imaging. Spontaneous calcium activity was recorded for 10 min (one frame every 8–10 s) in one 10-μm *z* stack plane. Fluorescence intensity (*F*) was exported as mean grey values in ImageJ. Signal decay was controlled by subtracting the mean fluorescence of the background (*F*_b). To estimate changes in intracellular calcium, Δ*F* was computed as (*F*_{cell} – *F*_b)/*F*₀, where *F*₀ represents the minimum *F* value per cell across the whole 10 min of recording from which *F*_b was subtracted. A Δ*F* > 1.2 was defined as a spike.

iDISCO. To optically clear fixed fused spheroids, we adapted the iDISCO protocol described in ref. 49. In brief, after fixation with 4% PFA for 3 h, spheroids were dehydrated with a day-long methanol (MeOH) dilution series (20% to 100% MeOH). Next, spheroids were incubated in 5% H₂O₂ overnight at 4 °C. The following day, the spheroids were rehydrated with a reverse MeOH dilution series and incubated overnight in 0.2% Triton X, 20% DMSO, 0.3 M glycine/PBS at 37 °C. The spheroids were then blocked with 0.2% Triton X, 10% DMSO, 6% goat serum/PBS at 37 °C for 2 days, followed by a heparin treatment for 2 h (PTwH: 0.2% Tween-20, 10 μg ml⁻¹ heparin/PBS) to reduce non-specific antibody binding. The spheroids were next incubated with a chicken anti-GFP (1:1,500; GeneTex: GTX13970) antibody for two days in PTwH with 5% DMSO and 3% goat serum at 37 °C. After a day-long wash series with PTwH, a secondary antibody diluted in PTwH, 3% goat serum was added for an additional two days at 37 °C. After two days of PTwH washes, the spheroids were cleared by a three-step tetrahydrofuran (THF) series (80%, 100%, 100% THF/H₂O), a 10 min dichloromethane step, and a short incubation in dichloromethane. The cleared spheroids were stored and imaged in dichloromethane on a Leica SP8 confocal microscope.

Real-time quantitative PCR (qPCR). mRNA was isolated using the RNeasy Mini kit and RNase-Free DNase set (Qiagen), and template cDNA was prepared by reverse transcription using the SuperScript III First-Strand Synthesis SuperMix for qRT-PCR (Life Technologies). qPCR was performed using Sybr Green (Roche) on a ViiA7 machine (Applied Biosystems, Life Technologies). Data was processed using the QuantStudio RT-PCR software (Applied Biosystems). Primers used are listed in Supplementary Table 2.

Single-cell gene expression (BD Resolve system). To capture transcriptomic information of hiPS-cell-derived hCS and hSS (IS condition) single cells, we used the BD Resolve system (BD Genomics) as previously reported with modifications¹³. Multiple hCS or hSS at day 105 of differentiation were combined and dissociated enzymatically into single cells and processed in one batch. Single-cell capture was achieved by random distribution of a single-cell suspension across >200,000 microwells through a limited dilution approach. Beads with oligonucleotide barcodes were added to saturation so that a bead was paired with a cell in a microwell. Cell-lysis buffer was added so that poly-adenylated RNA molecules hybridized to the beads. Beads were collected into a single tube for reverse transcription. Upon cDNA synthesis, each cDNA molecule was tagged on the 5' end (that is, the 3' end of a mRNA transcript) with a molecular index and cell label indicating its cell of origin. Whole transcriptome libraries were prepared using the BD Resolve single-cell whole-transcriptome amplification workflow. In brief, second strand cDNA was synthesized, followed by ligation of the adaptor for universal amplification. Eighteen cycles of PCR were used to amplify the adaptor-ligated cDNA products. Sequencing libraries were prepared using random priming PCR of the whole-transcriptome amplification products to enrich the 3' end of the transcripts linked with the cell label and molecular indices.

Sequencing libraries were quantified using a High Sensitivity DNA chip (Agilent) on a Bioanalyzer 2100 and the Qubit High Sensitivity DNA assay (Thermo Fisher Scientific). 1.5 pM of the library for each sample was loaded onto a NextSeq 500 system and sequenced using High Output sequencing kits (75 × 2 bp) (Illumina).

The BD Resolve analysis pipeline was used to process sequencing data (.fastq files). Cell labels and molecular indices were identified, and gene identity was determined by alignment against the gencode comprehensive hg19 reference. A table containing molecule counts per gene per cell was the output. 7,663 and 4,983 cells were identified for hCS and hSS, respectively, with an average number of reads of around 14,800, an average of about 3,710 molecules and around 1,700 number genes detected per cell with average molecular index coverage (that is, the number of times a molecule was sequenced) of around 2. A total of 34,242 genes were detected across all cells. Cells with mitochondrial gene (with a gene symbol starting with *MT*) content >25%, were discarded, retaining 7,126 and 4,712 cells for hCS and hSS (IS condition), respectively. Pseudogenes were removed. The distribution of reads per single cell is shown in Extended Data Fig. 2m. For visualization and clustering, the data tables of the two libraries were concatenated, and the combined table was further reduced to retain only the most variable genes using the method outlined in ref. 50, yielding 1,102 genes. *t*SNE projection of the data was performed using default parameters¹⁴. To determine the set of genes

contributing to the separation of cell clusters, differential gene expression analysis (DEseq) based on negative binomial distribution⁵¹ was conducted to compare gene expression profiles in cells in each cluster versus those in the rest of the dataset. Genes were ranked by smallest *P* values (expressed in terms of $-\log_{10}$) and the list of significantly over-represented genes with $-\log_{10}(P) < 10$ of each cluster is provided as Supplementary Table 3. Patterns of expression for the top 25 genes in each cluster are shown in Extended Data Fig. 2e–l). A very small group of hCS-derived cells clustered with the GABAergic interneuron subdomain, and differential gene expression indicated that these cells expressed *TBR1*, *RELN*, *PAX6* and *CALB2*.

Single-cell RNA sequencing (Smart-seq2). To assess the gene expression of *Dlx1/2b::eGFP⁺* cells in the hSS and in the hCS of fused hSS–hCS, we used a single-cell RNA-sequencing assay adapted from the Smart-seq2 protocol reported in ref. 52. In brief, hSS and hCS that had been fused for around 15 days were separated with a scalpel blade and dissociated independently as described. Single cells were isolated by FACS into a 96-well PCR plate containing 5 μ l of lysis buffer containing 0.04% Triton X-100 (10%, Sigma-Aldrich BioUltra), 0.1 μ l recombinant RNase inhibitor (TaKaRa), 1 μ l Oligo-dT30VN (10 μ M), 1 μ l of 10 mM dNTP mix (Fermentas) and nuclease-free H₂O at a final volume of 5 μ l. A known number of internal RNA control (ERCC) was added to the lysis master mix to estimate the technical variability between the wells of the same plate and between plates. Reverse transcription and PCR amplification were performed using the parameters described in ref. 52. The quality of the cDNA library was checked using a High-Sensitivity DNA chip (Agilent Bioanalyzer). Libraries were prepared using the Nextera XT library prep kit (96 index primers, Illumina). Because the Nextera XT kit is very sensitive to the concentration of cDNA, we screened pre-amplified cDNA libraries from all plates using the Qubit dsDNA HS Assay kit and used 125 pg cDNA from each positive well to further process the tagmentation and indexing. Twelve additional PCR cycles were performed to further enrich for pre-amplified tagged DNA. The quality of the tagged library was checked using the High-Sensitivity Bioanalyzer chip. The final pooled library was diluted to 2 nM using the elution buffer (Qiagen), and 10 pM was loaded on an Illumina HiSeq 2500 instrument for sequencing. Libraries were sequenced to obtain 50-bp single-end reads (TruSeq Rapid kit, Illumina) with eight additional cycles for indexing. On average, we obtained 2 million pass filter reads per single cell (Extended Data Fig. 6c). We considered a gene expressed if there were at least 10 reads detected for that gene. Cells that expressed more than 1,000 genes and <10% mitochondrial RNAs were kept for analysis. To avoid bias during FACS from RNA contamination from the glutamatergic neurons on the hCS side of the fused hSS–hCS, we analysed *STMN2⁺* cells that did not express *SLC17A6* or *SLC17A7*. To control for technical noise, we used a quantitative statistical analysis⁵³ to detect biological variable genes and used them for further analysis. To cluster and visualize the cells, we used the tSNE method in the computational software package Seurat⁵⁴.

Array tomography. Array tomography was used to collect high-resolution images of synapses within neural spheroids using previously published protocols^{11,55}. In brief, fused hSS–hCS were fixed in 4% PFA in PBS. To preserve GFP fluorescence, the tissue was dehydrated with up to 70% alcohol only, with processing through 50% ethanol, 70% ethanol, 1:3 70% ethanol:LR White Resin (LRW, medium grade, SPI supplies) and LRW overnight before embedding in LRW. The embedded tissue was sectioned into ribbons of 70-nm-thick sections (around 30 sections per ribbon) and each ribbon was immunostained in 2–3 rounds of staining with the antibodies eluted after each round. The following primary antibodies were used for immunostaining: anti-GFP (chicken, 1:200, Genetex, 13970), anti-SYN1 (rabbit, 1:500, Cell Signalling, 5297S), anti-PSD95 (rabbit, 1:200, Cell Signalling, 3450S), anti-VGUT1 (guinea pig, 1:5,000, Millipore, AB5905), anti-gephyrin (mouse, 1:100, BD Biosciences, 612632), anti-VGAT (guinea pig, 1:200, Synaptic Systems, 131004), anti-VGAT (mouse, 1:200, Synaptic Systems, 131011), anti-GFAP (chicken, 1:300, Aves), anti-MAP2 (guinea pig, 1:1,000, Synaptic Systems, 188004). Sections were visualized on a Zeiss Axio Imager.Z1 upright fluorescence microscope using AxioVision software (rel 4.7, Zeiss). Images were processed and registered using Fiji/ImageJ with standard and custom plugins (<https://code.google.com/archive/p/smithlabsoftware/>). Fiji/ImageJ was used for volume reconstruction.

Electrophysiology. Sections of hCS, hSS (day 96–141) or fused hSS–hCS (29–53 days after fusion) for physiological recordings were obtained using an approach we previously described¹¹. In brief, spheroids were incubated in bicarbonate-buffered aCSF at 23 °C and equilibrated with a mixture of 95% O₂ and 5% CO₂. The aCSF solution contained: 126 mM NaCl, 26 mM NaHCO₃, 10 mM glucose, 2.5 mM KCl, 1.25 mM NaH₂PO₄, 1 mM MgSO₄ and 2 mM CaCl₂. Slicing was performed using a Leica VT1200 vibratome. Immediately after sectioning, slices were moved to a circulation chamber containing oxygenated aCSF at 32 °C.

For patch-clamp recording, cells were identified by the presence of a fluorescent reporter using an upright Axoscope II microscope (Zeiss). Recording electrodes

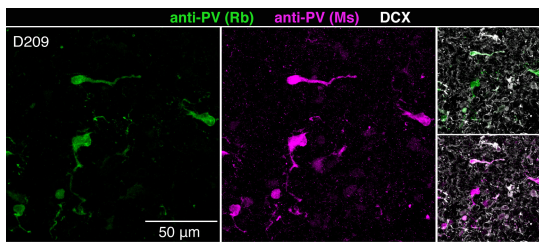
of borosilicate glass had a resistance of 4–6 M Ω when filled with internal solution. A low Cl[−] internal solution was used to distinguish between EPSCs and IPSCs containing: 145 mM K-gluconate, 0.1 mM CaCl₂, 2.5 mM MgCl₂, 10 mM HEPES, 0.2 mM EGTA, 4 mM Na-phosphocreatine. Cl[−] reversal was calculated to be at −91 mV according to the Nernst equation. A high Cl[−] internal solution was used to measure IPSCs in a subset of unfused hSS containing: 135 mM CsCl, 10 mM HEPES, 10 mM EGTA, 3 mM MgATP, 0.3 mM GTP. The Cl[−] reversal potential was calculated to be 0 mV according to the Nernst equation. IPSCs were blocked by application of the GABA_A receptor antagonist gabazine (10 μ M, Abcam), which was added to the superfused aCSF. EPSCs were blocked by application of the glutamate receptor antagonist kynurenic acid (1 mM, Abcam), which was added to the superfused aCSF. Electrical stimulation was delivered using a bipolar tungsten electrode (FHS) placed 200–400 μ m away from a recorded neuron. Stimulations were delivered to slices for 0.1 ms at 300 μ V and separated by at least 10 s. Inward EPSCs and outward IPSCs were recorded by filling the patch pipette with a low chloride internal solution ($E_{Cl} = -90$ mV) and holding the cell at −40 mV, which is near the midpoint between E_{Cl} and $E_{K/Na}$. Notably, the average shape of spontaneous IPSCs recorded in hSS displayed a prolonged decay as compared to the average EPSCs recorded from hCS, as is commonly observed in cortical neurons⁵⁶ (Extended Data Fig. 4b).

Data were collected using a 1550A digitizer (Molecular Devices), a 700B patch-clamp amplifier (Molecular Devices) and acquired with the pClamp 10.6 software (Molecular Devices). Recordings were filtered at 10 kHz. Synaptic recordings were analysed using custom software developed by J.R.H. (Wdetecta). Action potentials were analysed using custom MATLAB (MathWorks) programs. IPSCs and EPSCs were detected on the basis of their direction and shape. We calculated the first time derivative of the current recording and set a detection threshold that was twice the baseline for each trace. Detected responses were then evaluated to confirm the detection accuracy.

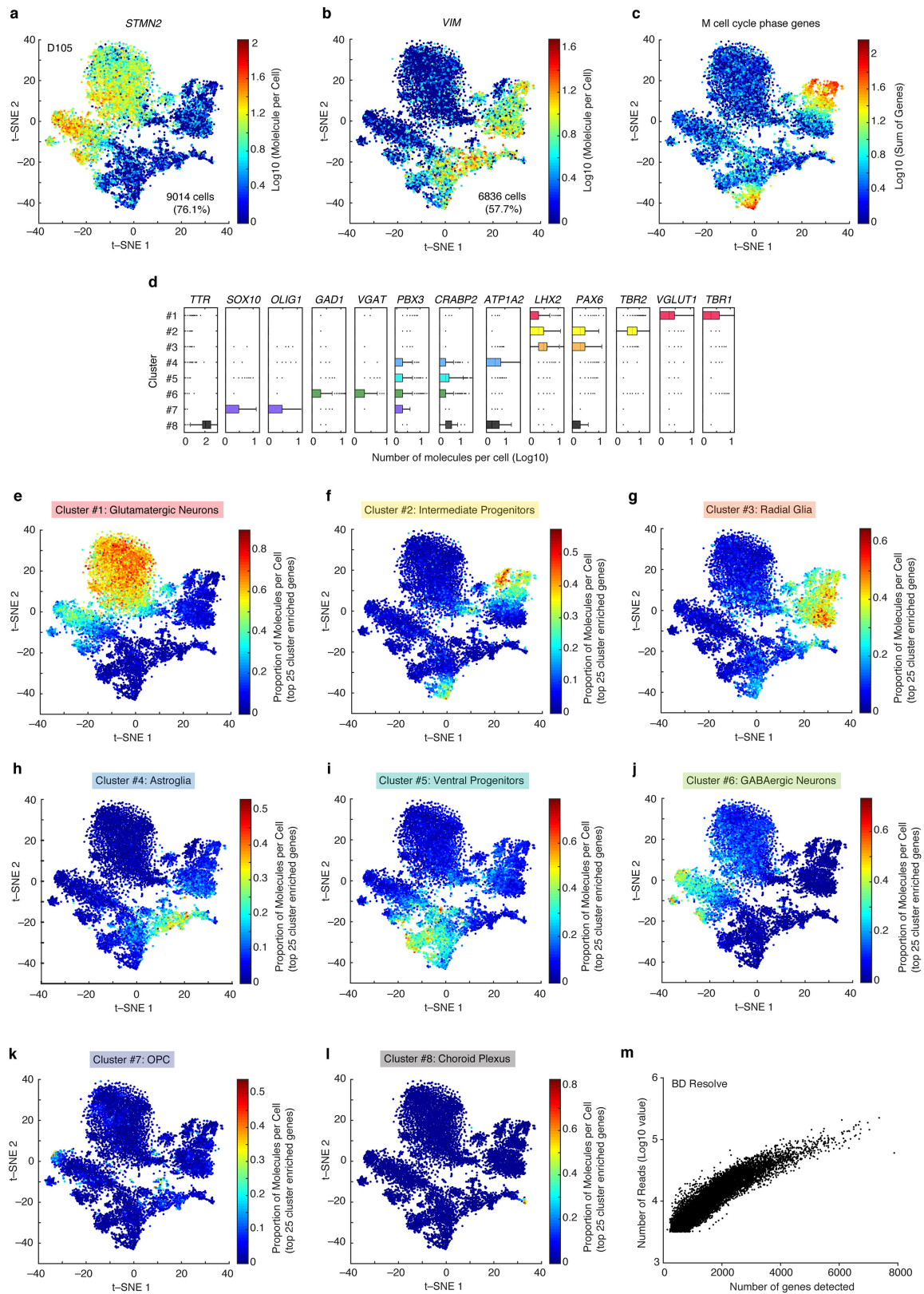
Statistics. Data are presented as mean \pm s.e.m., unless otherwise indicated. Distribution of the raw data was tested for normality of distribution; statistical analyses were performed using the Student's *t*-test, Mann–Whitney *U*-test, χ^2 test or ANOVA with post hoc tests as indicated. Sample sizes were estimated empirically or on the basis of power calculations. Blinding was used for all analyses comparing patients and control samples.

Data availability. Gene expression data are available in the Gene Expression Omnibus (GEO) under accession numbers GSE93811 (BD Resolve) and GSE96045 (Smart-seq2). The data that support the findings of this study are available on request from the corresponding author.

1. Yazawa, M. *et al.* Using induced pluripotent stem cells to investigate cardiac phenotypes in Timothy syndrome. *Nature* **471**, 230–234 (2011).
2. Gallego Romero, I. *et al.* A panel of induced pluripotent stem cells from chimpanzees: a resource for comparative functional genomics. *eLife* **4**, e07103 (2015).
3. Birey, F., Andersen, J. & Paşca, S. P. Generation and assembly of forebrain spheroids from human pluripotent stem cells. *Protoc. Exch.* <http://dx.doi.org/10.1038/protex.2017.044> (2017).
4. Deverman, B. E. *et al.* Cre-dependent selection yields AAV variants for widespread gene transfer to the adult brain. *Nat. Biotechnol.* **34**, 204–209 (2016).
5. Zhang, Y. *et al.* Purification and characterization of progenitor and mature human astrocytes reveals transcriptional and functional differences with mouse. *Neuron* **89**, 37–53 (2016).
6. Venkataramanappa, S., Simon, R. & Britsch, S. *Ex utero* electroporation and organotypic slice culture of mouse hippocampal tissue. *J. Vis. Exp.* (97), e52550 (2015).
7. Matsuda, T. & Cepko, C. L. Electroporation and RNA interference in the rodent retina *in vivo* and *in vitro*. *Proc. Natl Acad. Sci. USA* **101**, 16–22 (2004).
8. Lui, J. H. *et al.* Radial glia require PDGFR α –PDGFR β signalling in human but not mouse neocortex. *Nature* **515**, 264–268 (2014).
9. Renier, N. *et al.* iDISCO: a simple, rapid method to immunolabel large tissue samples for volume imaging. *Cell* **159**, 896–910 (2014).
10. Macosko, E. Z. *et al.* Highly parallel genome-wide expression profiling of individual cells using nanoliter droplets. *Cell* **161**, 1202–1214 (2015).
11. Anders, S. & Huber, W. Differential expression analysis for sequence count data. *Genome Biol.* **11**, R106 (2010).
12. Picelli, S. *et al.* Smart-seq2 for sensitive full-length transcriptome profiling in single cells. *Nat. Methods* **10**, 1096–1098 (2013).
13. Brennecke, P. *et al.* Accounting for technical noise in single-cell RNA-seq experiments. *Nat. Methods* **10**, 1093–1095 (2013).
14. Satija, R., Farrell, J. A., Gennert, D., Schier, A. F. & Regev, A. Spatial reconstruction of single-cell gene expression data. *Nat. Biotechnol.* **33**, 495–502 (2015).
15. Micheva, K. D., Busse, B., Weiler, N. C., O'Rourke, N. & Smith, S. J. Single-synapse analysis of a diverse synapse population: proteomic imaging methods and markers. *Neuron* **68**, 639–653 (2010).
16. Jang, H. J. *et al.* The development of phasic and tonic inhibition in the rat visual cortex. *Korean J. Physiol. Pharmacol.* **14**, 399–405 (2010).

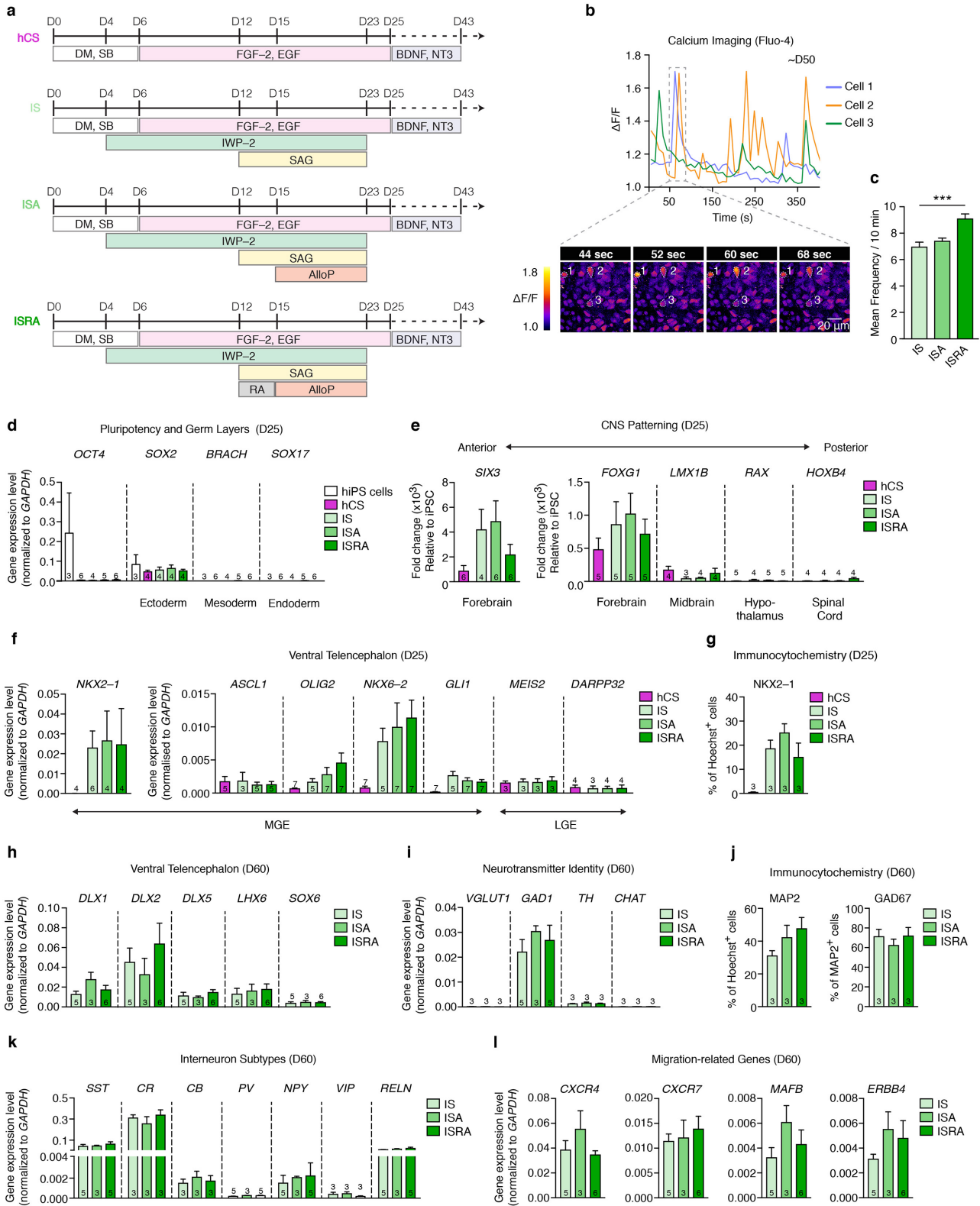


Extended Data Figure 1 | Immunostaining of hSS in cryosections showing parvalbumin neurons. Two anti-parvalbumin antibodies have been used to validate specificity to parvalbumin (PV); co-localization is shown with the neuronal marker DCX (day 209).



Extended Data Figure 2 | Single-cell gene expression of hCS and hSS at day 105 of differentiation. Single-cell gene expression analysis using the BD Resolve system ($n = 11,838$ cells). **a–c**, Distribution of expression of the neuronal marker *STMN2* (a), the progenitor marker *VIM* (b), and of a set of genes (c), which are associated with the M cell cycle phase (*AURKB*,

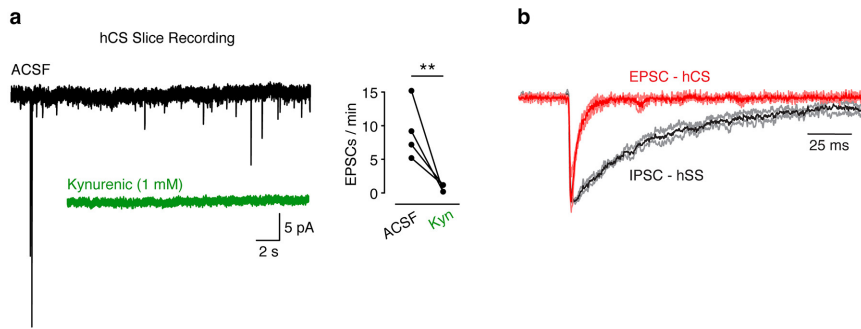
TPX2, *UBE2C*, *HMMR*, *TOP2A*, *CCNB1*, *NUSAP1*, *NUF2*, *CDC6*, *HIST1H4C*, *BIRC5* and *CKS2*). **d**, Box plots for genes enriched in each tSNE cluster shown in Fig. 1j. **e–l**, Top 25 genes in each of the eight clusters shown in Fig. 1j (proportion of molecules per cells). **m**, Scatter plot showing the number of genes detected versus the number of useful reads.



Extended Data Figure 3 | See next page for caption.

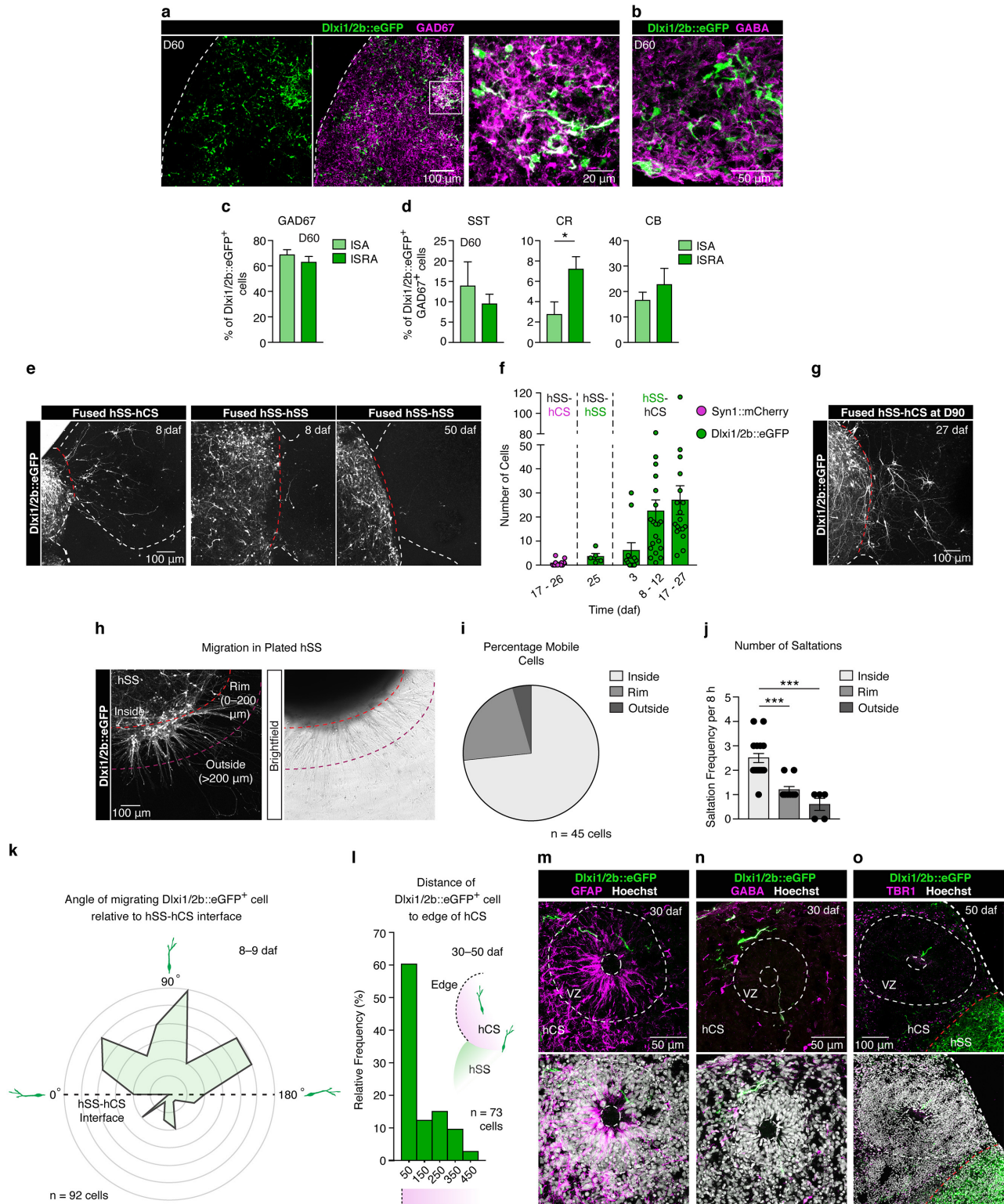
Extended Data Figure 3 | Characterization of hSS differentiation conditions. **a**, Schematic illustrating the differentiation conditions for deriving hCS or hSS: IS (IWP-2 and SAG), ISA (IWP-2, SAG and allopregnanolone (AlloP)) and ISRA (IWP-2, SAG, allopregnanolone (AlloP) and retinoic acid (RA)). Medium for all three conditions contained dorsomorphin (DM) and SB-431542 (SB), FGF2, EGF, BDNF and NT3 at the indicated time points. **b**, Representative traces of intracellular calcium measurements (Fluo-4) demonstrating spontaneous activity in hSS at around day 50 of differentiation. $\Delta F/F$ indicates the fluorescence intensity over baseline fluorescence. **c**, Average calcium spike frequency in three distinct hSS differentiation conditions: IS ($n = 114$ cells), ISA ($n = 327$ cells), ISRA ($n = 136$ cells); cells were derived from three hiPS cell lines; one-way ANOVA, $F_{3,719} = 5.86$, $***P < 0.001$. **d**, Gene expression (qPCR, normalized to *GAPDH*) levels, showing downregulation of *OCT4* and the lack of mesoderm (brachyury, *BRACH*) and endoderm (*SOX17*) markers following differentiation of hiPS cells into hCS and hSS conditions.

e, Gene expression (qPCR, fold change versus hiPS cells and normalized to *GAPDH*) levels, showing upregulation of forebrain markers (*SIX3* and *FOXG1*) but not midbrain (*LMX1B*), hypothalamus (*RAX*) or spinal cord (*HOXB4*) markers. **f**, Expression of ventral forebrain genes in hSS and hCS (qPCR, normalized to *GAPDH*) at day 25. **g**, Average percentage of the proportion of NKX2-1 by immunostaining in dissociated hCS or hSS at day 25. **h**, Expression of ventral forebrain genes in hSS (qPCR, normalized to *GAPDH*) at day 60. **i**, Expression of glutamatergic, GABAergic, dopaminergic and cholinergic neurotransmitter identity genes in hSS (qPCR, normalized to *GAPDH*) at day 60. **j**, Average percentage of the proportion of MAP2/Hoechst and GAD67/MAP2 by immunostaining in dissociated hSS at day 60. **k, l**, Expression of interneuron subtype genes and markers associated with interneuron migration in hSS (qPCR, normalized to *GAPDH*) at day 60. Number of hPS lines used indicated on each column. Data are mean \pm s.e.m.



Extended Data Figure 4 | Electrophysiological recordings of hCS and hSS. a, Representative EPSC traces of recordings from hCS neurons (sliced preparation) before (black) and during (green) exposure to the glutamate receptor blocker kynurenic acid (Kyn, 1 mM) (Mann–Whitney U -test,

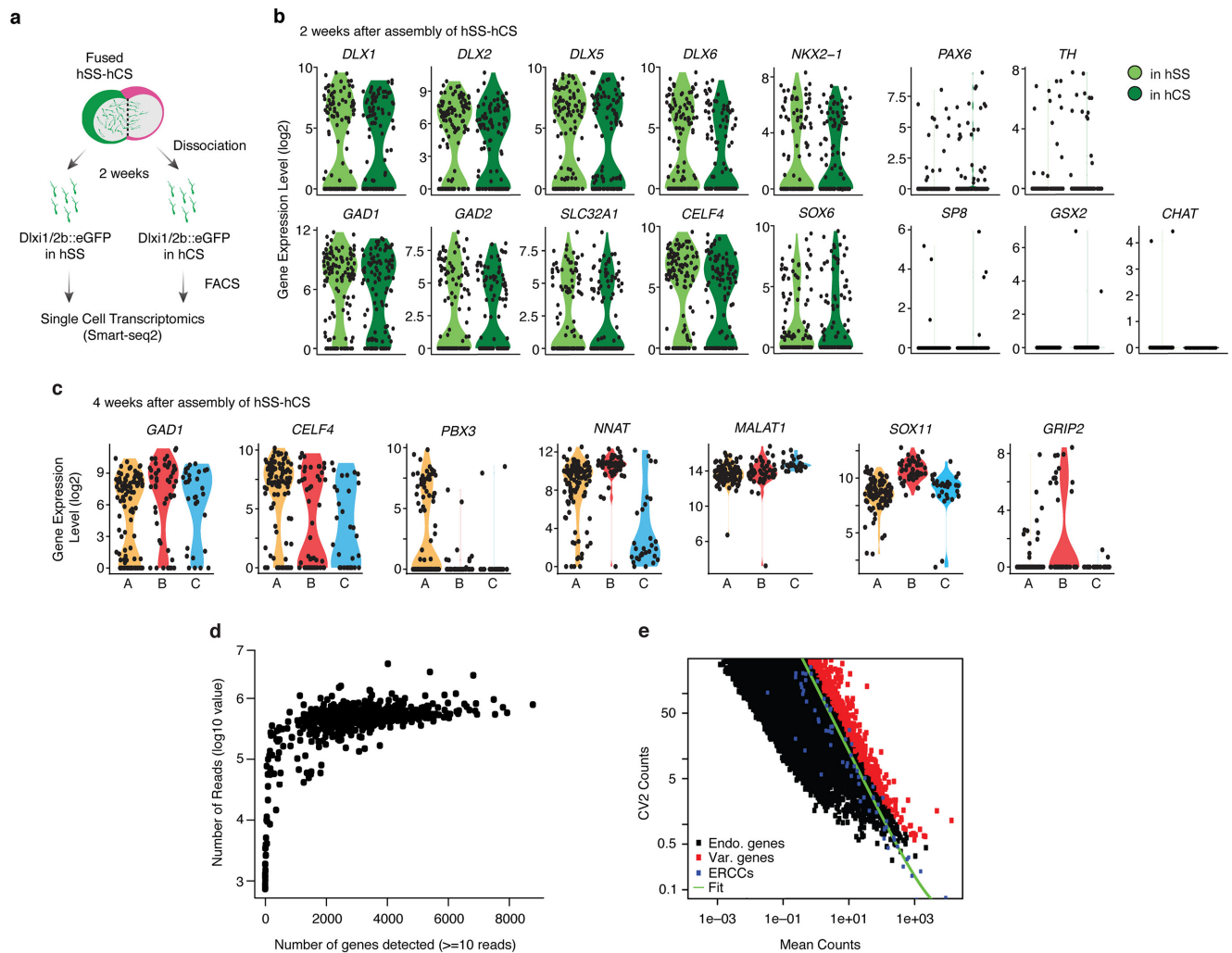
** $P = 0.007$). **b,** Overlap of averaged EPSCs (red) recorded in hCS neurons ($n = 6$ cells) and averaged IPSCs (black) recorded in hSS ($n = 5$ cells). Data are mean \pm s.d.



Extended Data Figure 5 | See next page for caption.

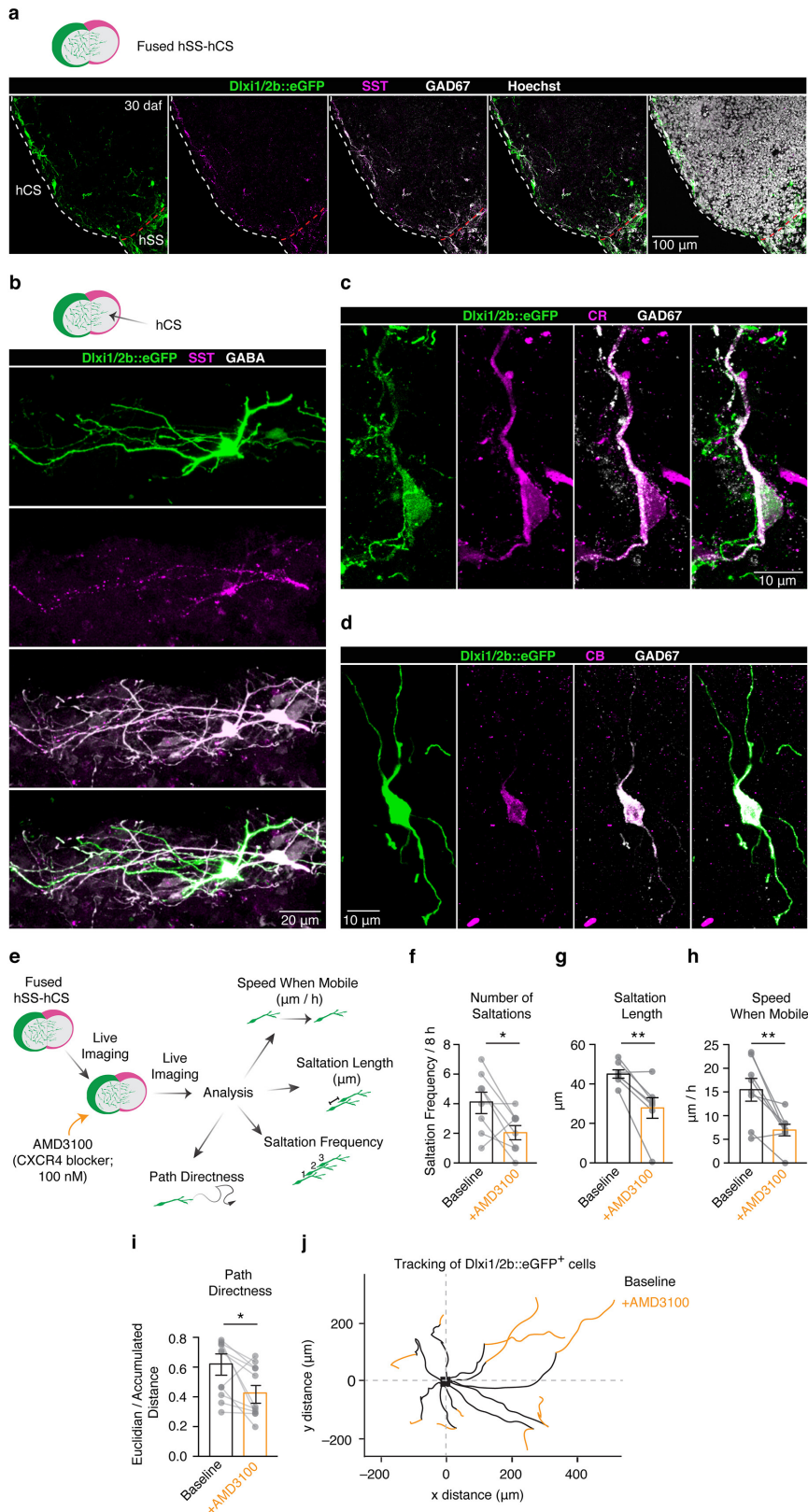
Extended Data Figure 5 | Migration of *Dlxi1/2::eGFP*⁺ cells in fused hSS–hCS. **a, b**, Representative immunostaining in cryosections of hSS showing co-expression of *Dlxi1/2::eGFP* and *GAD67* (**a**) or *GABA* (**b**). **c**, Quantification by immunostaining of the proportion of *Dlxi1/2::eGFP*⁺ cells that co-express *GAD67* in hSS derived using the ISA or ISRA condition ($n = 3$ hiPS cell lines; t -test, $P = 0.35$). **d**, Proportion of *Dlxi1/2::eGFP*⁺ and *GAD67*⁺ cells in hSS derived using the ISA or ISRA condition that co-express somatostatin (*SST*) (t -test, $P = 0.48$), calretinin (*CR*) (t -test, $*P = 0.04$) or calbindin (*CB*) (t -test, $P = 0.43$); $n = 3$ hiPS cell lines. **e**, Representative images of hSS–hCS at day 60 showing migration of *Dlxi1/2::eGFP*⁺ cells (from fluorescently labelled hSS) in fused hSS–hCS, but not in hSS–hSS over time. **f**, The number of *Dlxi1/2::eGFP*⁺ (hSS-derived) or *hSYN1::mCherry*⁺ cells (hCS-derived) that moved in hSS–hCS or hSS–hSS was quantified in snapshots of live, intact spheroids at different time points (from day 3 to 25). The values shown are the absolute number of cells that migrated to the other side (approximately the same area and thickness was imaged in each session); one-way ANOVA for cells at 17 days after assembly; $F_{2,32} = 8.24$, $P = 0.001$. **g**, Representative images of fused hSS–hCS at day 91 showing migration of *Dlxi1/2::eGFP*⁺ cells (from fluorescently labelled hSS) into fused hSS–hCS. **h**, Representative image of an hSS that was plated on a glass

coverslip and cultured for around 7 days. **i**, Percentage of *Dlxi1/2::eGFP* inside the coverslip-plated hSS, in the rim (0–200 μm) or beyond this region (>200 μm). **j**, Quantification of the number of saltations of *Dlxi1/2::eGFP*⁺ cells ($n = 32$ cells) inside the one-week coverslip-plated hSS, in the rim and outside this region (one-way ANOVA, interaction $F_{2,30} = 22.12$, $P < 0.001$; Bonferroni post hoc test, $***P < 0.0001$). **k**, Diagram showing the angle of movement of migrating *Dlxi1/2::eGFP*⁺ cells at 8–9 days after assembly of hSS–hCS. The angle was calculated between the leading process of *Dlxi1/2::eGFP*⁺ cells that have moved into hCS and the fusion interface ($n = 92$ cells from five hiPS cell lines). **l**, Histogram showing the distribution of the distance of migrated *Dlxi1/2::eGFP*⁺ cells relative to the edge of hCS in hSS–hCS at 30–50 days after assembly. The distance was measured in fixed 18- μm cryosections ($n = 73$ cells from two hiPS cell lines). **m–o**, Representative examples of migrated *Dlxi1/2::eGFP*⁺ cells in the hCS that moved within a ventricular zone-like region. The ventricular zone-like region contains GFAP-expressing cells, is surrounded by *TBR1*⁺ cells and the migrated cells show *GABA* expression. Supplementary Video 2 shows movement of *Dlxi1/2::eGFP*⁺ cells that is reminiscent of the ventricular-directed migration described in rodents.



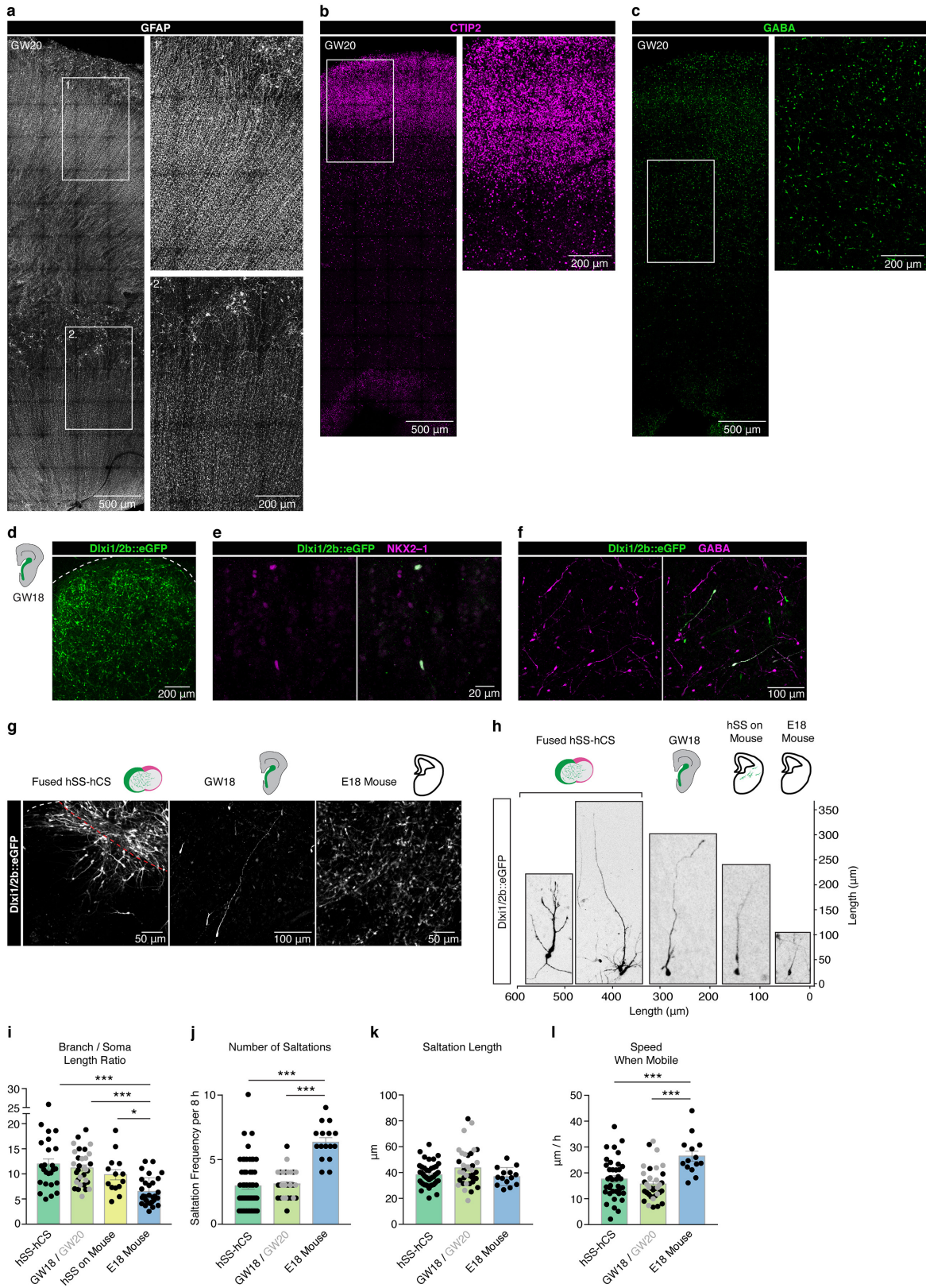
Extended Data Figure 6 | Single-cell gene expression of *Dlx1/2::eGFP*⁺ cells in hSS and hCS. **a**, Schematic showing the isolation by dissociation and fluorescence-activated cell sorting (FACS) of *Dlx1/2::eGFP*⁺ cells from hSS or hCS for single-cell transcriptional analysis. **b**, Violin plots showing expression in *Dlx1/2::eGFP*⁺ cells of selected genes associated with cortical, striatal and olfactory interneurons in hSS (light green, $n = 123$ cells) or hCS (dark green, $n = 106$ cells) at two weeks after assembly of hSS-hCS. **c**, Violin plots showing expression in *Dlx1/2::eGFP*⁺ cells (at four weeks after assembly of hSS-hCS) in clusters A, B, and C (likelihood ratio test; *GAD1*, *CELF4*: $P > 0.05$; *PBX3*:

$P < 1 \times 10^{-7}$ for A versus B and C; *NNAT*: $P < 1 \times 10^{-16}$ for C versus A and B, $P < 1 \times 10^{-16}$ for B versus A and C; *MALAT1*: $P < 1 \times 10^{-9}$ for C versus A and B; *SOX11*: $P < 1 \times 10^{-16}$ for B versus A and C, $P < 1 \times 10^{-9}$ for A versus B and C; *GRIP2*: $P < 1 \times 10^{-8}$ for B versus A and C). **d**, Scatter plot showing the number of genes detected (≥ 10 reads cut-off) versus the number of reads ($n = 410$ cells from combined single-cell RNA-sequencing experiments after two or four weeks of assembly in hSS-hCS). **e**, Graph illustrating biologically variable transcripts (red circles) and non-variable transcripts (black circles) along with the technical noise from the ERCC spike in RNAs (blue dots). Green line shows the technical noise fit.



Extended Data Figure 7 | Immunocytochemistry and pharmacology in fused hSS-hCS. a–d, Representative images of immunostainings for somatostatin (SST), GAD67, GABA, calretinin (CR) and calbindin (CB) in Dlx1/2::eGFP⁺ cells after migration in fused hSS-hCS. **e,** Schematic illustrating the pharmacological manipulation of Dlx1/2::eGFP⁺ cells that are migrating in hSS-hCS. **f–i,** Quantification of Dlx1/2::eGFP⁺ cell

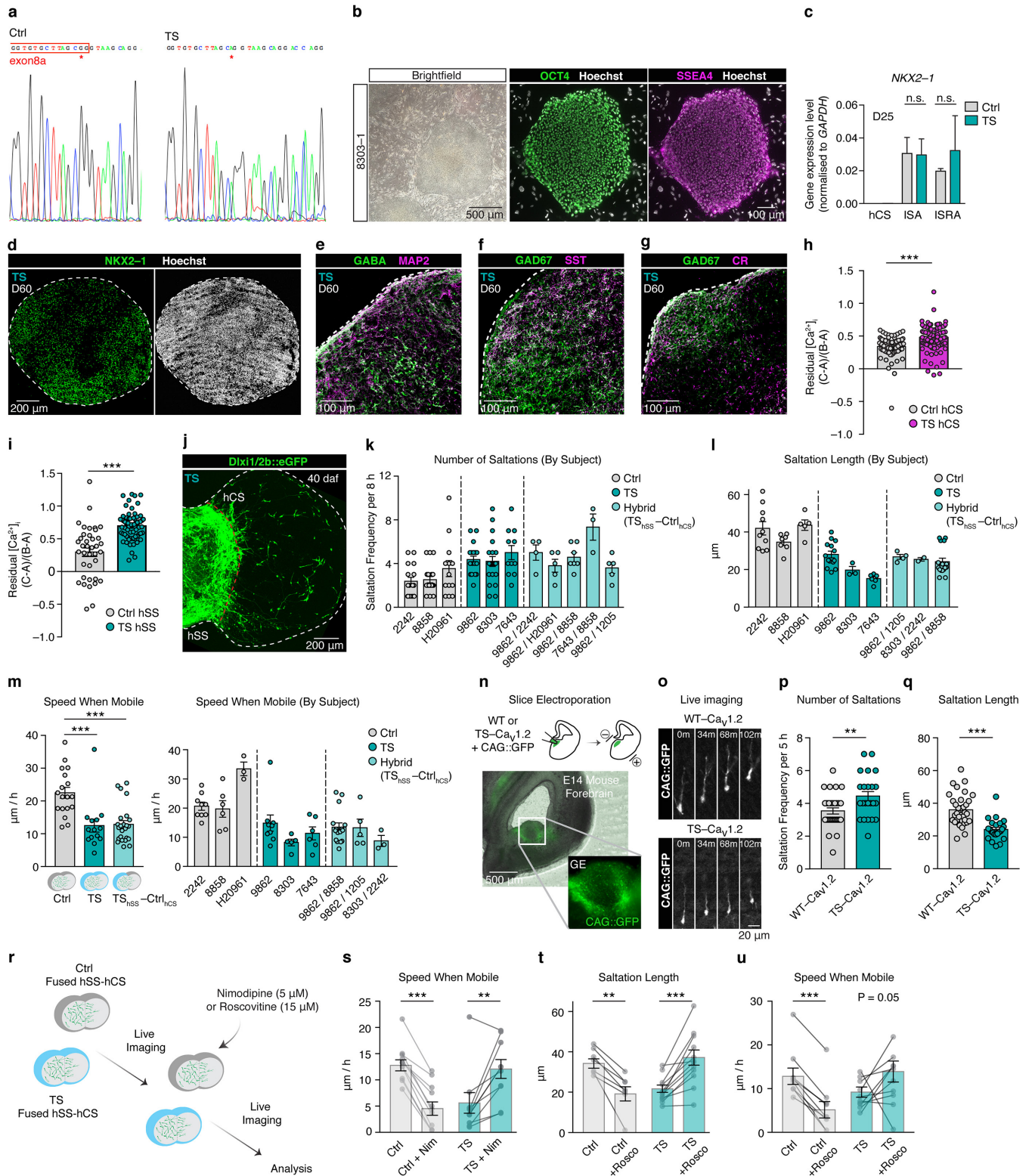
migration before and after exposure to 100 nM of the CXCR4 antagonist AMD3100 ($n = 8$ cells from two hiPS cell lines; paired t -tests, $*P = 0.03$ for number of saltations (**f**), $**P = 0.006$ for saltation length (**g**), $**P = 0.006$ for speed when mobile (**h**), $*P = 0.02$ for path directness(**i**)). **j,** Plot illustrating the trajectory of Dlx1/2::eGFP⁺ cells in fused hSS-hCS before and after exposure to AMD3100. Data are mean \pm s.e.m.



Extended Data Figure 8 | See next page for caption.

Extended Data Figure 8 | Migration of *Dlxi1/2::eGFP*⁺ cells in mouse and human forebrain slices versus hSS-hCS. **a–c**, Representative images of human fetal cortex at GW20 showing immunostaining with antibodies against GFAP (**a**), CTIP2 (**b**) and GABA (**c**). **d**, Representative image showing cell labelling with the *Dlxi1/2::eGFP* reporter in human forebrain at GW18 (six days after lentivirus infection). **e, f**, Representative images of immunostained cryosections of human tissue at GW18 showing co-localization of *Dlxi1/2::eGFP* with NKX2-1 (**e**) and GABA (**f**). **g**, Representative images showing cell labelling with the *Dlxi1/2::eGFP* reporter in hSS-hCS (nine days after assembly), in human forebrain (GW18) and in mouse slice cultures (E18). **h, i**, Comparison of *Dlxi1/2::eGFP*⁺ cell size and quantification of the ratio of soma diameter to the length of the leading process in fused hSS-hCS ($n = 25$ cells from four hiPS cell lines), human forebrain at GW18 ($n = 19$ cells, black) and

GW20 ($n = 15$ cells, grey), hSS-derived cells cultured on E14 mouse forebrain slices ($n = 14$ cells), and E18 mouse forebrain slices ($n = 30$ cells from two litters) (one-way ANOVA, interaction $F_{3,97} = 11.61$, $P = 0.001$; Bonferroni post hoc test $*P < 0.05$, $***P < 0.001$). **j–l**, Comparison of the number of saltations ($n = 56$ cells from two hiPS cell lines; one-way ANOVA, interaction $F_{2,103} = 29.27$, $P = 0.001$, Bonferroni post hoc test $***P < 0.001$), saltation length ($n = 44$ cells from three hiPS cell lines; one-way ANOVA, interaction $F_{2,91} = 3.0$, $P = 0.50$), speed when mobile ($n = 38$ cells from three hiPS cell lines; one-way ANOVA, interaction $F_{2,83} = 11.38$, $P = 0.001$, Bonferroni post hoc test $***P < 0.001$) for *Dlxi1/2::eGFP*⁺ in fused hSS-hCS, human fetal forebrain (GW18, $n = 19$ cells; GW20, $n = 15$ cells), and E18 mouse forebrain slices ($n = 14$ cells for saltation length and speed, $n = 16$ cells for number of saltations from two litters). Data are mean \pm s.e.m.



Extended Data Figure 9 | See next page for caption.

Extended Data Figure 9 | Derivation of TS hSS, migration and

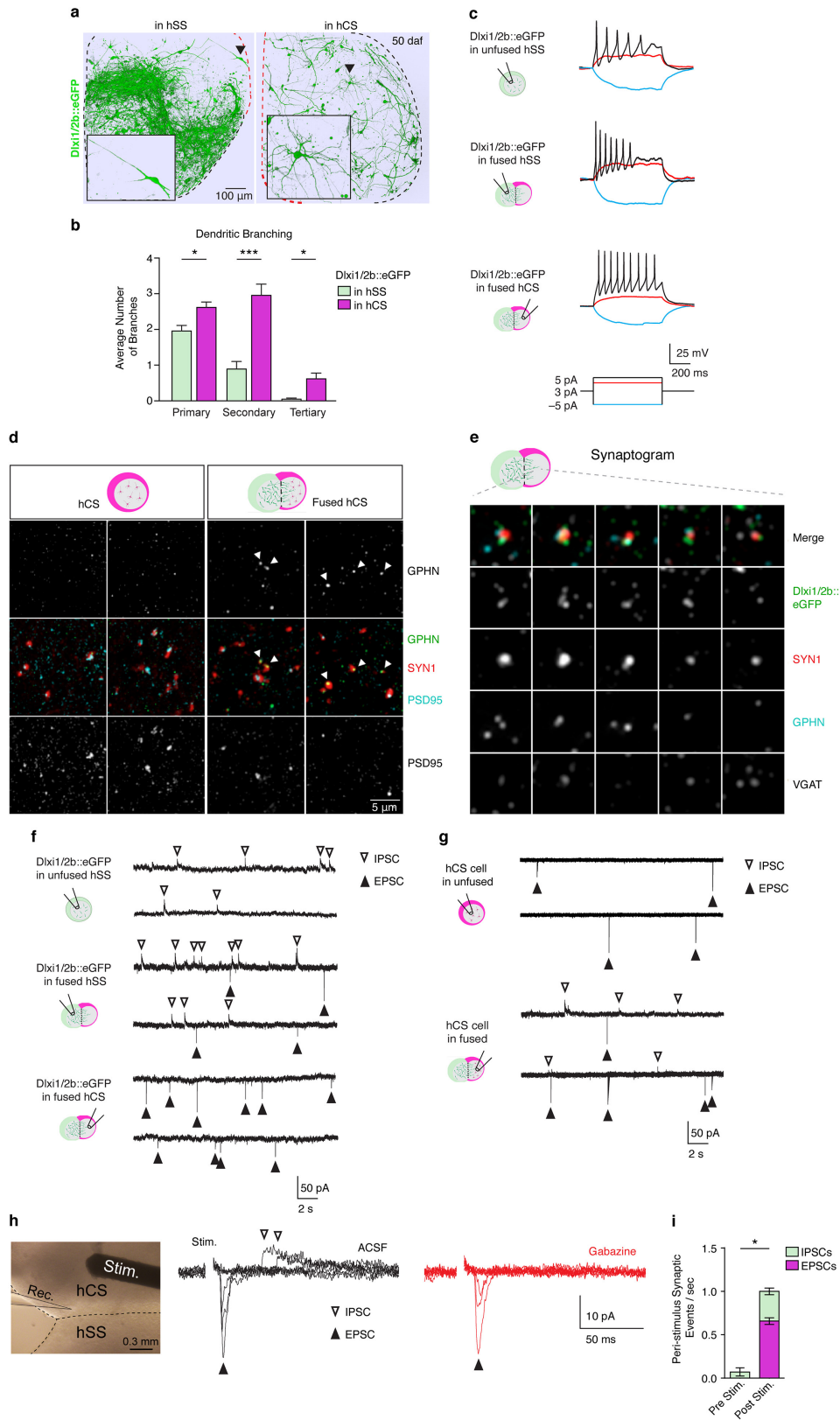
electroporation. a, Sequencing of PCR-amplified DNA showing the p.G406R mutation in exon 8a of *CACNA1C* in TS (subject 8303).

b, Representative images of hiPS cell colonies expressing pluripotency markers (OCT4, SSEA4) in one TS subject. **c**, Level of gene expression (qPCR, normalized to *GAPDH*) for *NKX2-1* showing no defects in ventral forebrain induction in TS (two-way ANOVA; interaction $F_{2,15} = 0.20$, $P = 0.81$; TS versus control $F_{1,15} = 0.16$, $P = 0.68$). n.s., not significant.

d–g, Representative images of immunostained cryosections of TS hSS (day 60) showing expression of *NKX2-1*, GABA, MAP2, GAD67, somatostatin (SST) and calretinin (CR). **h**, Calcium imaging (Fura-2) in dissociated hCS derived from TS subjects and controls (control, $n = 81$ cells from two subjects; TS, $n = 147$ cells from two subjects). Quantification of residual intracellular calcium ($[Ca^{2+}]_i$) following 67 mM KCl depolarization of control and TS cells in hCS cells. Residual $[Ca^{2+}]_i$ was calculated by dividing the plateau calcium (C – A) level by the peak calcium elevation (B – A) (t -test, $***P < 0.001$). **i**, Quantification of $[Ca^{2+}]_i$ following depolarization of control and TS cells in hSS (t -test, $***P < 0.001$).

j, Representative image of fused TS hSS–hCS showing *Dlxi1/2::eGFP* expression and migration. **k, l**, Quantification of the number of saltations and saltation length of *Dlxi1/2::eGFP* cells in fused hSS–hCS across multiple control and TS lines (related to Fig. 3d, e). **m**, Quantification of the speed when mobile of *Dlxi1/2::eGFP* cells in fused hSS–hCS (control, $n = 21$ cells from three hiPS cell lines derived from three subjects; TS, $n = 29$ cells from three hiPS cell lines derived from three subjects;

TS–control hybrid, $n = 12$ cells from three combinations of five hiPS cell lines from five subjects; one-way ANOVA with Dunnett's multiple comparison test, $***P < 0.001$). **n**, Electroporation of cDNA encoding the TS and wild-type (WT) $Ca_v1.2$ channels into slices of mouse E14 ganglionic eminences (GE). **o**, Representative example of time-lapse live cell imaging depicting the saltatory migration of GFP^+ cells in slices electroporated with CAG::GFP and either wild-type or TS *CACNA1C*. **p, q**, Quantification of the number of saltations (**p**, t -test, $**P < 0.01$) and saltation length (**q**, t -test, $***P < 0.001$) of GFP^+ cells in electroporated mouse forebrain slices (wild type, $n = 33$ cells; TS, $n = 23$ cells; from three litters). **r**, Schematic illustrating pharmacological manipulation of LTCCs during live cell imaging of fused hSS–hCS. **s**, Quantification of speed when mobile following exposure to the LTCC blocker nimodipine (5 μ M) (paired t -test; control, $n = 13$ cells from three hiPS cell lines derived from three subjects, $***P < 0.001$; TS, $n = 12$ cells from two hiPS cell lines derived from two subjects, $**P < 0.005$). **t**, Quantification of saltation length following exposure to roscovitine (15 μ M) (paired t -test; control, $n = 7$ cells from two hiPS cell lines derived from two subjects, $**P < 0.005$; TS, $n = 12$ cells from two hiPS cell lines derived from two subjects; $***P < 0.001$). **u**, Quantification of speed when mobile following exposure to roscovitine (15 μ M) (paired t -tests; control, $n = 9$ cells from two hiPS cell lines derived from two subjects, $***P < 0.001$; TS, $n = 12$ cells from two hiPS cell lines derived from two subjects; $P = 0.05$). Data are mean \pm s.e.m.



Extended Data Figure 10 | See next page for caption.

Extended Data Figure 10 | Characterization of *Dlxi1/2::eGFP*⁺ cells after migration. **a**, Representative images of three-dimensional reconstructed *Dlxi1/2::eGFP*⁺ cell morphologies before and after migration from hSS into hCS. **b**, Quantification of dendritic branching of *Dlxi1/2::eGFP*⁺ cells in hSS ($n = 58$ cells) and in hCS ($n = 55$ cells) of fused hSS–hCS (two-way ANOVA; interaction $F_{2,129} = 11.29$, $P < 0.001$; Bonferroni post hoc test $*P < 0.05$, $***P < 0.001$). **c**, Representative examples of action potentials (slice recordings) in *Dlxi1/2::eGFP*⁺ cells in unfused hSS, in hSS of fused hSS–hCS and in hCS after migration in fused hSS–hCS. **d**, Array tomography showing expression of the GABAergic synapse marker GPHN (green) colocalized with SYN1 (red) in hCS of fused hSS–hCS but not in unfused hCS; the glutamatergic marker PSD95 (cyan) colocalized with SYN1 is found in both fused and unfused hCS (equal volumes 1.2- μm deep). **e**, Array tomography of a

Dlxi1/2::eGFP⁺ synapse illustrating the colocalization with SYN1 (red), GPHN (cyan) and VGAT (white); five consecutive 70-nm sections ($3 \times 3 \mu\text{m}$). **f**, Representative examples of whole-cell voltage-clamp recordings of IPSCs and EPSCs from *Dlxi1/2::eGFP*⁺ cells in unfused hSS, in fused hSS–hCS or after migration in hCS. **g**, Representative examples of whole-cell voltage-clamp recordings of IPSCs and EPSCs in cells recorded from unfused hCS cells and fused hCS cells. **h**, Electrical stimulation and patch-clamp recording in fused hSS–hCS showing evoked EPSCs and IPSCs before (black) and after exposure to 10 μM gabazine (red). **i**, Average peri-stimulus synaptic events (IPSCs and EPSCs) in *Dlxi1/2::eGFP*⁺ cells recorded in the hCS side of fused hSS–hCS before and after electrical stimulation (paired t -test, $*P < 0.05$). Data are mean \pm s.e.m.